1   **Warm and Moist Air Intrusions into Winter Arctic: A Lagrangian view on the near-surface energy budgets**

2   Cheng You[1], Michael Tjernström[1], Abhay Devasthale[2]

3   [1]Department of Meteorology & Bolin Centre for Climate Research, Stockholm University, Stockholm, Sweden.

4   [2]Remote Sensing Unit, Research and Development Department, Swedish Meteorological and Hydrological
5   Institute, Norrköping, Sweden.

7   *Correspondence to*: Cheng You (cheng.you@misu.su.se)

8   **Abstract**. In this study, warm and moist air intrusions (WaMAI) over the Arctic Ocean sectors of Barents, Kara,
9   Laptev, East Siberian, Chukchi and Beaufort Seas in recent 40 winters (from 1979 to 2018) are identified from
10   ERA5 reanalysis using both Eulerian and Lagrangian views. The analysis shows that WaMAIs, fuelled by Arctic
11   blocking, causes a relative surface warming and hence a sea ice reduction by exerting positive anomalies of net
12   thermal irradiances and turbulent fluxes to the surface. Over Arctic Ocean sectors with land-locked sea ice in
13   winter, such as Laptev, East Siberian, Chukchi and Beaufort Seas, total surface energy budget is dominated by
14   net thermal irradiance. From a Lagrangian perspective, total water path (TWP) increases linearly with the
15   downstream distance from the sea ice edge over the completely ice-covered sectors, inducing almost linearly
16   increasing net thermal irradiance and total surface energy-budget. However, over the Barents Sea, with an open
17   ocean to the south, total net surface energy-budget is dominated by the surface turbulent flux. With the energy in
18   the warm-and-moist air continuously transported to the surface, net surface turbulent flux gradually decreases
19   with distance, especially within the first 2 degrees north of the ice edge, inducing a decreasing but still positive
20   total surface energy budget. The boundary-layer energy-budget patterns over the Barents Sea can be categorized
21   into three classes: radiation-dominated, turbulence-dominated and turbulence-dominated with cold dome,
22   comprising about 52%, 40% and 8% of all WaMAIs, respectively. Statistically, turbulence-dominated cases with
23   or without cold dome occur along with one order of magnitude larger large-scale subsidence than the radiation-
24   dominated cases. For the turbulence-dominated category, larger turbulent fluxes are exerted to the surface,
25   probably because of stronger wind shear. In radiation-dominated WaMAIs, stratocumulus develops more strongly
26   and triggers intensive cloud-top radiative cooling and related buoyant mixing that extends from cloud top to the
27   surface, inducing a thicker well-mixed layer under the cloud. With the existence of cold dome, fewer liquid water
28   clouds were formed and less or even negative turbulent fluxes could reach the surface.

29   Keywords: Arctic climate, Stratocumulus, Trajectories, Warm and moist air intrusions

30   **1. Introduction**

31   In recent decades, rapidly intensified Arctic warming has been observed (Cohen et al., 2014; Graversen et al.,
32   2008a; Screen et al., 2018), which has become known as Arctic amplification (Serreze and Francis 2006).
33   Accompanying this warming has been a dramatic melting of Arctic sea ice (Screen and Simmonds, 2010;
34   Simmonds, 2015; Simmonds and Li, 2021). Particularly over the Barents Sea, a rapid warming rate, as well as a
35   remarkable sea ice decrease, is found, which may have impacts on the extreme cold winters in Eurasia (Kim et
36   al., 2014; Kim and Son, 2016; Li et al., 2021; Luo et al., 2019; Mori et al., 2014; Overland et al., 2011; Petoukhov
37   and Semenov, 2010; Rudeva and Simmonds, 2021; Tang et al., 2013).

Arctic amplification is likely a consequence of many contributing processes and a detailed attribution to different factors is yet to be performed. The most commonly implied mechanism is the so-called albedo feedback, based on the consideration that open water absorbs considerably more solar radiations than sea ice, which would accelerate Arctic warming (Kim et al., 2019). However, Arctic amplification is the strongest in winter, when the sun is mostly absent and the albedo by definition plays no role at all. This suggests that atmospheric energy transport by warm-and-moist intrusions (WaMAI) may play an important role for Arctic amplification, especially in winter. The positive trend in number of winter WaMAIs can statistically explain a substantial part of the surface air temperature and sea-ice concentration trends in the Barents Sea (Luo et al., 2017a; Nygård et al., 2020; Woods and Caballero, 2016).

Most of these studies deal with winter and focus either on the dynamical mechanisms resulting in WaMAIs, or on the effects of WaMAIs on the Arctic climate system conducted from an Eulerian perspective by retrieving composite mean of WaMAIs properties (Liu et al., 2018), or calculating regressions between different metrics (Gong and Luo, 2017). In recent years it has been increasingly argued that the concept of Lagrangian air mass transformation is necessary for studying WaMAIs (Ali and Pithan, 2020; Komatsu et al., 2018; Pithan et al., 2018). Trajectories have been utilized to study the origin and transport pathway of winter WaMAIs (Papritz et al., 2022), as well as the thermodynamic processes along the trajectories (Papritz, 2020). A method using trajectories to analyze WaMAIs from a Lagrangian perspective was designed by You et al. (2020) and tested on a summer WaMAI event described in Tjernström et al. (2015). This method was utilized to build a climatology of summer WaMAIs (You et al., 2021).

In this paper, we use this method to explore winter WaMAIs over several sectors of the Arctic Oceans: the Barents, Kara, Laptev, East Siberian, Chukchi and Beaufort Seas. Over the Barents Sea, sea ice concentration is decreasing and the near-surface atmosphere south of the ice edge is heated by comparatively warm open water. In contrast, for the Laptev, East Siberian, Chukchi and Beaufort Seas, the ocean surface is almost completely frozen to the coast and the insulation effect by sea ice suppresses heat transfer between ocean and atmosphere. We will attempt understanding the distinctions between the ocean sector with open water and those with land-locked sea ice by comparing surface and boundary-layer energy-budgets from both Eulerian and Lagrangian perspectives.

2. Data and method

2.1 Data

We use the latest reanalysis from European Centre for Medium-Range Weather Forecast (ECMWF), ERA5 (Hersbach et al., 2020) in this study. For the detection and Eulerian analysis of WaMAIs in recent 40 winters (DJF from 1979 to 2018), we use the reanalysis dataset at a 6-hourly temporal and $0.75°$ horizontal resolution. This includes the vertically integrated northward water vapor flux (f_w), sea ice concentration (SIC), 500-hPa geopotential height (GH_{500}), 2m air temperature (T_{2m}), 850-hPa temperature (T_{850}), total water path (TWP), liquid water path (LWP), ice water path (IWP) and precipitation rate (PRCP). For the Lagrangian analysis we also use ERA5 3D wind field at a 6-hourly resolution for the calculations of air-mass trajectories during WaMAIs, in the same way as described in You et al. (2020, 2021). We additionally interpolate energy-budget terms with forecast data from ERA5 at the higher temporal resolution (1-hourly). This includes surface net solar (F_{sw}) and

75 thermal (F_{lw}) irradiances, the surface sensible (F_{sh}) and latent heat fluxes (F_{lh}), as well as the 1-hourly temperature

76 tendencies due to different model physics extracted at model levels.

77   Utilizing ERA5 reanalysis introduces uncertainty, especially for anything that comes from parameterized

78 model physics such as cloud parameters and the energy budget. Large upward residual heat flux biases exist

79 among all reanalysis and turbulent heat flux over the sea ice are also poorly simulated in all seasons (Graham et

80 al., 2019). ERA5 has larger warm bias in winter, especially when the surface temperature is under $-25°C$. Sea

81 ice thickness is thinner in ERA5 because of the larger warm bias and higher precipitation (Wang et al., 2019). In

82 the data assimilation, the main variables in a reanalysis are constrained by observations and in-situ observations

83 over the central Arctic Ocean are sparse, especially in winter. The loss of all visible wavelengths in passive remote

84 sensing in winter also makes many satellite products less trustworthy. However ERA-Interim, the predecessor of

85 ERA5, generally performs best among the available reanalysis datasets, especially for the wind (Lindsay et al.,

86 2014) and substantial progress has been made in data quality and diagnostic techniques during last few decades

87 (Mayer et al., 2019). However, it would be not possible to analyze air mass transformation climatologically on

88 the energy-budgets along the trajectories of winter WaMAIs in any other way than relying on reanalysis. Here,

89 we alleviate uncertainty in two ways; first, by averaging over a large number of cases and second, by considering

90 anomalies rather than actual mean values. Avoiding single case studies reduces random errors, while considering

91 anomalies reduces systematic errors.

92 **2.2. WaMAI Detection**

93 Clouds and moisture are integral and important parts of the Arctic surface and boundary-layer energy budgets and

94 relative humidity in the Arctic boundary layer is almost always high (Andreas et al., 2002; Persson et al., 2002).

95 A particular warm air intrusion may carry less moisture than a typical moist intrusion, but a typical

96 moist intrusion will certainly carry warm air into the Arctic. We therefore name these events as 'warm and

97 moist air intrusions', identify and quantify them with the vertically integrated northward moisture flux, f_w,

98 separately over the ocean sectors of Barents, Kara, Laptev, East Siberian, Chukchi and Beaufort Seas (Figure 1).

99 Among these sectors, winter SIC only varies substantially with the time over the Barents and Kara Seas. North of

100 $80°N$ in the Barents Sea, SIC has a statistically significant regression coefficient with f_w (Figure 2a). locations that

101 pass a $p < 0.05$ Student's t-test (stippled in Figure 2a) are considered the sensitive region. For the remaining

102 sectors, all sea ice covered locations are considered sensitive regions since they do not display winter variability

103 in SIC. The mean f_w over each sensitive region, $\overline{f_w}$, are approximately normally distributed (Figure 2b and d). We

104 define a WaMAI as a continuous period when $\overline{f_w} > 0$ (red lines in Figure 2c and e) with a maximum larger than

105 the 95-percentile of the distribution of all values of $\overline{f_w}$. The portion of a WaMAIs when $\overline{f_w}$ is larger than the 95-

106 percentile are moreover considered extreme moist intrusions (EMIs; blue line in Figure 2c and e); note that each

107 WaMAI can only include one EMI. The onset and terminal time of a WaMAI is taken at the nearest minimum

108 values of $\overline{f_w}$, or zero of $\overline{f_w}$.

109   Similar as You et al.(2021, 2020), ensembles of two day forward and backward trajectories at different

110 altitudes are calculated for each WaMAI over all ocean basins, using the trajectory algorithm from Woods et al.

111 (2013). Over each ocean sectors and for each WaMAI, we select a launch point along a latitude circle where the

112 T850 is the largest. The latitude circle of 75 °N (blue lines in figure 2a) is used for all ocean sectors, except for

the Barents Sea where 80 °N (red line in figure 2a) is used. Forward (backward) trajectories are also terminated where they start to track southward (northward). Hence, we only capture the part of each trajectory that continuously tracks northwards. Finally, the terminal points of selected trajectories have to be at least 5° north of the sea-ice edge, defined as where SIC exceeds 15% and reach 80 °N (85 °N for the Barents Sea sector). Trajectories are calculated at several different heights, every 100 m, from 300 m to 800 m and vertical profiles of the various variables are then extracted from ERA5, from the surface to 2 km, by interpolation in time and space along each of these trajectories. The final vertical cross-section for each WaMAI is the ensemble average of the results along all trajectories initialised at different heights. For the 40 winters in this study, 87 (131) WaMAIs are detected over the ocean sectors with open ocean (land-locked sea ice) for a total of 218 WaMAIs.

It is to be noted that both the temporal and spatial resolutions would influence the accuracy of the trajectory calculation (Stohl et al., 1995). However, the increase of only temporal or spatial resolution does not necessarily improve the accuracy of trajectory calculation (Draxler, 1987). In this study, we calculate the trajectories 2 days forward and backward, instead of calculating 4 days trajectory at once. Furthermore, we also calculate the ensembles of trajectories at different heights to decrease the error introduced by vertical interpolation from pressure level to geometric height.

2.3. Energy Budgets

As shown in Eq. 1, total surface energy-budget (F_{total}) is contributed by surface net solar irradiance (F_{sw}), surface net thermal irradiance (F_{lw}), surface turbulent sensible heat fluxes (F_{sh}) and surface turbulent latent heat fluxes (F_{lh}). Note that all surface net energy fluxes contributing to a surface warming are considered positive. Individual terms in Eq. 1 are also interpolated from ERA5 at each 0.5-degree interval in latitude along the trajectories.

$$F_{total} = F_{sw} + F_{lw} + F_{sh} + F_{lh} \quad (1)$$

We also evaluate the cloud longwave radiative effects (CRE) ($F_{lw\_CRE} = F_{lw\_all\_sky} - F_{lw\_clear\_sky}$), using the same method. $F_{lw\_all\_sky}$ is the surface net thermal irradiance, considering the actual clouds presence, while $F_{lw\_clear\_sky}$ is clear-sky counterpart, assuming clouds were not present.

For the atmospheric energy budget calculations, we also extract the temperature tendencies due to different model physics from ERA5, where we can resolve all terms in the thermal equation (Eq. 2). As shown in Eq. 2, the total temperature tendency T_t of an air-mass in a WaMAI is contributed by heating/cooling from the divergence of shortwave irradiance ($\frac{\partial T}{\partial t}_{sw}$), longwave irradiance ($\frac{\partial T}{\partial t}_{lw}$) and vertical turbulent heat flux ($\frac{\partial T}{\partial t}_{TH}$) and the latent heat of condensation in cloud formation ($\frac{\partial T}{\partial t}_{LH}$). In a Lagrangian view, the advection tendencies are by definition zero, while in an Eulerian view, the total tendencies would additionally be balanced by temperature advection. All these terms are also interpolated along the trajectories as previously discussed (also see You et al. 2020, 2021).

$$T_t = \frac{\partial T}{\partial t}_{sw} + \frac{\partial T}{\partial t}_{lw} + \frac{\partial T}{\partial t}_{LH} + \frac{\partial T}{\partial t}_{TH} \quad (2)$$

146   Note that while the surface energy budget depends on the surface fluxes, the atmospheric energy budget depends

147   on the vertical gradient of fluxes.**3. Results**

148   **3.1 Large-scale Features**

149   EMIs were identified in the Arctic ocean basins of Barents, Kara, Laptev, East Siberian, Chukchi and Beaufort.

150   Figure 3 (4) shows the composite of all EMIs over the Barents (Beaufort) Sea, representing the large-scale features

151   of winter EMIs over ocean sectors with open ocean (land-locked sea ice). Both figure 3a and 4a show one pair of

152   negative and positive GH_{500} anomalies with a large geopotential height gradient in between, generating an

153   intensive f_w anomaly directed into the Arctic (Figure 3c, 4c), enhancing temperature advection (Figure 3b, 4b) and

154   cloud formation (Figure 3d, 4d), consistent with previous studies (Tjernström et al. 2015; Overland and Wang

155   2016; Gong and Luo 2017; Johansson et al., 2017; Sedlar and Tjernström 2017; Messori et al. 2018; Cox et al.

156   2019; You et al., 2021). Unlike over the Barents Sea, where the TWP anomaly is dominated by LWP (Figure 4d

157   and 4e), TWP over the Beaufort Sea is dominated by IWP. These features in the GH_{500}, T_{850} and TWP anomalies

158   are also found in all other ocean basins (Figure S1, S3, S5, S7).

159   As warm and moist air is advected into the Arctic over the Barents Sea, it interacts with the cool ice

160   surface through turbulence and radiation, enforcing positive F_{sh}, F_{lh} and F_{lw} anomalies at the surface (Figure 5c,

161   5d and 5e). The F_{sh} anomaly reaches > 60 W m^{-2} over open water near the Norwegian coast, tapering off northward

162   over the ice all the way to the pole. The pattern of F_{lh} anomaly is similar to that of F_{sh} south of 80°N, but decreases

163   to nearly zero over the sea ice north of 80°N. Positive LWP and IWP anomalies in figure 3d and 3e, extending

164   from the coast to the north pole along the path of the EMIs, also affects the surface energy-budget with a positive

165   F_{lw} anomaly (Figure 5c). This relation between F_{lw} anomaly and winter EMIs over the Barents Sea is also

166   discussed in other climatological analyses (Gong et al., 2017; Gong and Luo, 2017). In total, these anomalies in

167   the surface-energy fluxes sum up to a positive F_{total} anomaly, inducing decreased SIC (Figure 5b).

168   Similar surface energy-budget pattern is also found over the Beaufort Sea (Figure 6) and other ocean

169   sectors with land-locked sea ice (Figure S2, S4, S6, S8), but with some differences. The anomaly in F_{total} over the

170   Barents Sea is dominated by F_{sh}, while F_{total} anomaly over the Beaufort Sea is dominated by F_{lw}. The magnitudes

171   of F_{sh}, F_{lh} and F_{total} anomalies over the Beaufort Sea are less half the magnitude of those over the Barents Sea,

172   especially south of 80°N and hence induce four times less SIC decrease. As EMIs occur over the Beaufort Sea,

173   positive F_{sh}, F_{lh}, F_{total}, F_{lw}, LWP and IWP anomalies and negative SIC anomaly is found. However, negative F_{sh},

174   F_{lh}, F_{total}, F_{lw}, LWP and IWP anomalies and positive SIC anomalies could also be found over the Barents Sea

175   sector, while some WaMAIs from the Beaufort Sea pass through the pole and become cold spells over the Barents

176   Sea (Figure 4 and 6).

177   Table 1 summarizes the averaged surface energy-budgets over sea ice across the six basins. Except for

178   the Barents Sea, F_{lw} anomalies are almost twice larger than F_{sh} anomalies. Since F_{sw} anomalies can be ignored

179   in winter, the F_{lw} anomalies dominate F_{total}. However, over the Barents Sea, F_{sh} anomalies are almost twice larger

180   than F_{lw} anomalies and contribute to more than 50% of F_{total} anomalies. Over the Barents and Chukchi Sea,

181   positive F_{sh} anomalies are statistically significant, which is not the case for any of the other sectors. Except for

182   the Laptev Sea, positive F_{total} and F_{lw} anomalies are statistically significant. Here, if the mean values of these

surface energy-budget terms are positive and greater than their standard deviation, then we consider they are statistically significantly positive.

The composites of large-scale pattern discussed above are extracted from the stronger EMI events to generate a clear signal, however, these may not necessarily represent the general pattern of all WaMAIs. Therefore, linear regressions of daily averaged GH, T_{850}, SIC, F_{total}, F_{sh}, F_{lh}, F_{sw} and F_{lw} anomaly against the time series of daily averaged $\bar{f}_w$ over the sensitive regions in recent 40 winters were calculated separately for all the examined ocean basins. All the regressed fields have similar pattern as their counterparts in Figures 3~6, implying a similar relationship for all days but at smaller magnitudes. Since the regressions confirm the conclusions, we will consider only the Barents and Beaufort Seas as an example of ocean sector with open ocean and land-locked sea ice, respectively (Figure 7 and 8).

3.2 The Surface Energy-budget

In this section, we will explore the transformation of temperature inversion, cloud formation and surface energy-budget along the trajectories of warm-and-moist air masses over ocean basins with open water and land-locked sea ice, respectively, by compositing the heights to the maximum specific humidity (h_{sh}), temperature (h_t) and vertical temperature gradient (h_{t_z}), along with TWP, LWP, IWP, precipitation rate (PRCR) and surface energy-budget terms (F_{sh}, F_{lh}, F_{total}, F_{lw}) from all detected WaMAIs.

Over the completely ice-covered sea sectors such as the Laptev, East Siberia, Chukchi and Beaufort Seas, strong temperature inversion develops with cloud formation below, as the warm-and-moist air propagates over the sea ice. In this case, h_{sh} is higher than h_t, and both are higher than h_{t_z} (Figure 9a). From the ice edge and onward up to 10 degrees north of the ice edge, h_{sh}, h_t and h_{t_z} increase almost linearly, by 30-40 m per degree latitude (Figure 9a) as the inversion is lifted. TCW and PRCP also increase northward, although more slowly for the first two degrees, in total by 6 g m^{-2} and 0.4 mm day^{-1} per degree latitude, respectively, implying that stratocumulus develop continuously along the trajectories (Figure 9b, c). The increasing TWP is mainly due to the increase in IWP since LWP is almost constant along the trajectories (Figure 9b). The increase of h_{t_z} is comparable to that of summer WaMAIs, while the increase in TWP is about half of that of summer WaMAIs (You et al., 2021), since less moisture is available for cloud development in winter (Figure 4c). The gradual increase of h_{t_z}, a manifestation of increased boundary-layer mixing, leads to a reduction in near-surface gradients. Since the turbulent heat fluxes at the surface depend on these gradients, the F_{sh} anomaly decreases gradually at a rate of 1.5 W m^{-2} per degree latitude (Figure 10a). Simultaneously, the F_{lw} anomaly increases almost linearly by 2.5 W m^{-2} per degree latitude, while F_{lh}, the smallest contributor to F_{total}, is almost constant along the trajectories (Figure 10a). The increase in F_{lw} along trajectories is due to an increasing cloud radiative effects by the evolving stratocumulus clouds; F_{lw_CRE} increases at a similar rate as F_{lw} (Figure 10b). From 0 to 2 degrees north of the sea ice edge, the F_{total} anomaly is dominated by the F_{sh} anomaly, while farther north it is dominated by F_{lw} anomaly (Figure 10a). Generally, F_{total} anomaly increases with the distance from the sea ice edge at a rate of 1 W m^{-2} (degree latitude)$^{-1}$ and this increasing trend is dominated by F_{lw} anomaly (Figure 10a).

Over the Barents Sea, with open warm water south of the ice edge, h_t and h_{sh} also increase nearly linearly but at a 1.6 times larger rate than those over ocean sectors with land-locked sea ice, however, starting at considerably smaller values (Figure 9d). The maximum values of h_t and h_{sp} here are comparable to the minimum values over the completely ice-covered sectors, implying that WaMAIs over the Barents Sea develops a shallower well-mixed layer and hence bring the moist and warm air closer to the surface. However, the temperature inversion over the Barents Sea is too weak to be easily identified with the metrics used above. Unlike for the sectors with land-locked sea ice, TWP and PRCR are constant with downwind distance from the ice edge, varying slightly around 150 g m^{-2} and 7 mm day^{-1} (Figure 9e, f). As a consequence, F_{lw} anomaly and F_{lw_CRE} along the trajectories (Figure 10c, d) are nearly constant with northward distance. Although TWP remains quasi-constant, LWP (IWP) decreases (increases) at a rate of -6 g m^{-2} (+6 g m^{-2}) along the trajectories (Figure 9e). From 0 to 4 degrees north of the sea ice edge, TWP is contributed by LWP and IWP in about equal parts, while from 4 degrees north of the sea ice edge and onward, TWP gradually becomes dominated by IWP. The F_{sh} anomaly decreases fast by nearly 50% over the first two degrees from the sea ice edge (Figure 10c). From 2 to 10 degrees north of the sea ice edge, the decrease is more moderate at a rate of 4 W m^{-2} per degree latitude (Figure 10c), which is still faster than that over the completely frozen ocean sectors. However, the F_{sh} anomaly is still larger than the largest corresponding value for the completely frozen ocean sectors, even ten degrees north of the ice edge (Figure 10a). This is likely due to the much warmer upstream conditions over the open ocean. The large thermal contrast between open ocean and sea ice surface contributes to the stable atmospheric layer over the sea ice surface and rapidly reducing F_{sh} anomaly, while the decrease of F_{sh} anomaly with downstream distance is due to the slowly reducing temperature gradient resulting from the turbulent mixing. Similar decreasing trends are also present for F_{lh} and F_{total} anomaly (Figure 10c). From 2 to 10 degrees north of the sea ice edge, they decrease at a rate of 1 and 5 W m^{-2} per degree latitude, respectively (Figure 10c). Within 5 degrees north of the sea ice edge, F_{total} anomaly is dominated by F_{sh}, while downstream the turbulent heat flux ($F_{sh} + F_{lh}$) anomaly becomes comparable to F_{lw} anomaly and contribute almost equally to F_{total} anomaly (Figure 10c).

Without the presence of solar radiation in winter, the variation of F_{total} anomaly over the Barents Sea is dominated by F_{sh} anomaly (Figure 10a), while it is dominated by F_{lw} anomaly over ocean sectors with land-locked sea ice (Figure 10c). This distinction between ocean sectors with and without open ocean upstream can be explained by the stronger air-sea interaction over the Barents Sea (Kim et al., 2019). Before the air-mass is advected in over the sea ice, it is heated and moistened by the ocean and consequently, exerts greater turbulent heat fluxes to the surface as it suddenly enters over the sea ice (Figure 10c). Cloud formation happens already upstream over the warm water and in a much deeper PBL and is hence not much affected by the advection over sea ice. Instead a much shallower well-mixed layer forms as the air enters over the ice, and the larger vertical gradients resulting from the large temperature difference across the ice edge gives rise to larger F_{sh}. This dominance of turbulent heat fluxes remains until the halfway along the trajectories.

3.3 The Boundary-layer Energy-budget

As discussed in previous sections, cloud formation as part of the air-mass transmission can exert large variability on the surface energy-budget. Here, we focus on the cloud effects on the boundary-layer energy-budget. For each WaMAI, the boundary-layer energy-budget terms are evaluated and interpolated along the trajectory and analyzed on a case-by-case basis, categorizing patterns into four main categories: a) lifting temperature inversion (INV); b)

radiation-dominated (RAD); c) turbulence-dominated (TBL); and d) turbulence-dominated with cold dome (TCD). Some typical cases are shown in figure 11-14 respectively for these four categories, illustrating different boundary-layer energy-budgets in each category, while conceptual summary graphs of all the different categories are summarized in Figure 15. The boundary-layer energy-budget pattern plotted this way is very variable from case to case, mainly because the northward component of the advection is differently from case to case; also, the location of the ice edge is different from year to year. Hence, some trajectories are long but reach less far north while other are shorter and still reaches further north. In the vertical, the cases are also subject to different subsidence, affecting the PBL growth. We therefore have yet to come up with a workable normalization that would allow an ensemble average of all the cases.

Almost all WaMAIs over ocean sectors with land-locked sea ice feature a boundary-layer energy-budget pattern of category INV. Similar to category TBL for summer WaMAIs (You et al., 2021), category INV is characterized by increasingly lifting temperature inversion and continuously stratocumulus development near the inversion. Different from the ocean sectors with land-locked sea ice, clouds during WaMAIs over the ocean sector with an upstream open ocean (e.g. Barents Sea) form at the altitude of ~1 km, above the warm-and-moist air-masses. The boundary-layer energy-budget here is categorized into three categories (RAD, TBL, TCD). Category RAD is characterized by stronger cloud-top radiative cooling and related buoyant mixing, while category TBL is characterized by more intensive surface turbulent mixing. Category TCD is similar to category TBL excluding a cold dome over the high Arctic. The boundary-layer energy-budget patterns are categorized by manually checking case by case if they have the typical characteristics of each categories. Their launch time and launch longitudes are listed in table S1. WaMAIs over the Kara Ocean sector are characteristic of both ocean sector with land-locked sea ice and open ocean. Some WaMAIs behave as typical for the Barents Sea, while some behave like for the other sectors with land-locked sea ice.

Note that unlike radiation and condensation/evaporation, turbulence does not generate heating/cooling by itself. Instead, it heats/cools air locally by redistributing heat from one altitude to another through mixing within the column. Also, note that the temperature tendencies discussed below are only those that are due to model physics in a Lagrangian view, while in an Eulerian framework, they would be balanced by advection (not shown). In an absolute sense the boundary layer always undergoes a gradual cooling during the advection over the sea ice.

3.3.1 Lifting temperature inversion (INV)

In this category turbulent heating and cooling dominate the boundary-layer energy-budget (Figure 11e and 11h), even though stratocumulus develops along the trajectories and affects the radiative processes (Figure 11a and f). Turbulent mixing transports heat from the upper to the lower parts of the PBL, hence cooling the upper and warming the lower parts of the PBL (Figure 11h). Since the turbulent mixing persists along the trajectories, the well-mixed layer below the inversion continuously deepens northward (Figure 11b), while the inversion and the cloud top are gradually lifted (Figure 11a). This supports the hypothesis from Tjernström et al. (2019), that the surface inversion formed at the sea ice edge is eroded progressively downstream, by cloud-top cooling and surface turbulent mixing, and eventually the boundary layer must transform into the often observed well-mixed cloud-capped boundary layer (Brooks et al., 2017; Graversen et al., 2008; Morrison et al., 2012; Pithan et al., 2014; Sotiropoulou et al., 2014; Tjernström et al., 2012; Tjernström and Graversen, 2009). Even though this hypothesis

296   was originally posed for summer WaMAIs, it is also applicable to winter WaMAIs over completely frozen ocean

297   sectors; see Figure 15a.

298   Clouds are relatively thin and radiative cooling near the cloud top is therefore weak (Figure 11f) and

299   only in a few cases the magnitude of radiative cooling is comparable to the turbulent cooling. Generally, in this

300   category, turbulent heating is larger than radiative heating as well as latent heating, and hence boundary-layer

301   warming is dominated by turbulence, but since turbulence only redistribute heat inside the PBL, as a whole it is

302   gradually cooled as the warm air progresses northward.

303   **3.3.2 Radiation-dominated (RAD)**

304   Over the Barents Sea, the maximum air temperature (Figure 12a, 13a, 14a) and specific humidity (Figure 12d,

305   13d, 14d) over open ocean south of the ice edge are always located right above the sea surface as a result of the

306   strong air-sea interaction and are also typically larger than those over ocean sectors with land-locked sea ice. As

307   this air-mass, considerably affected by air-sea interaction, is advected over the sea ice, different stories take place.

308   Around 8% of all WaMAIs over the Barents Sea belong to category RAD (Table 2). In this category, the

309   total temperature tendencies are forced by radiative processes. For this category, the large-scale subsidence is an

310   order of magnitude smaller than that in category TBL (Table 3, CONV) and LWP is three times larger than that

311   in category TCD (Table 3, LWP), suggesting that the stratocumulus develops more intensively in category RAD

312   (Figure 12a). With larger values of LWP, longwave radiation is effectively emitted at the cloud top like a black

313   body, exerting large cooling rates with maximum reaching -16 K day^{-1}. However, unlike the cloud formation in

314   category INV, here clouds always already form south of the ice edge over the open water and few clouds develop

315   in the near-surface inversion. In the cloud, heat is redistributed with warming at the cloud top and cooling in the

316   lower PBL by buoyant mixing driven by cloud-top longwave radiative cooling (Figure12h). The turbulent cooling

317   layer in the PBL interior is apparently thicker than the turbulent warming layer whose absolute value of heating

318   rate is considerably more intensive (Figure12h). As shown in figure 12h, the buoyant mixing can access the surface

319   and induce a thicker well-mixed layer below the stratocumulus (Figure 12b). As precipitation constantly erodes

320   the cloud, buoyant mixing continuously provides moisture for the cloud development from the moister air below

321   and hence cloud development as well as the cloud top cooling is maintained.

322   Meanwhile, the value of maximum temperature and specific humidity is decreasing gradually along the

323   trajectory, indicating that the heat and moisture within the warm-and-moist air is consumed continuously by the

324   cloud formation and surface turbulent mixing. For this category, F_{lw} is comparable to those of category TBL and

325   TCD (Table 3), and increases almost linearly along the trajectory (Figure 16d1) due to the enhancing TWP (Figure

326   16c1). F_{sh} and F_{lh} are generally smaller than those of category TBL since stronger mixing weakens vertical

327   gradients in the PBL and hence suppresses the surface turbulent heat flux (Table 3). The decreasing rates of F_{sh}

328   and F_{lh} from 0 to 2 degrees north of the sea ice edge are larger than for categories TBL and TCD as a result of

329   stronger buoyant mixing in the PBL (Figure 16a1), while onwards, their decreasing rates are smaller than those

330   for the other two categories since the lifting rates of h_t and h_{sp} are dramatically slowed down (Figure 16b1); see

331   Figure 15b.

332   **3.3.3 Turbulence-dominated (TBL)**

52% of WaMAIs over the Barents Sea belong to the turbulence dominated category. The variation of surface energy-budget along the trajectory (Figure 16 a2, b2 and c2) is similar to the mean variation of WaMAIs from all categories showed in figure 10c and 10d. Subsidence for WaMAIs in this category is typically a factor of three larger than that in category RAD and it is statistically significantly positive (Table 3, CONV). Consequently, clouds in this category do not develop as intensively as in category RAD and hence the radiative cooling rate at the cloud top is considerably smaller. The boundary-layer energy-budget is mainly dominated by turbulent heating near the surface. As warm-and-moist air is advected into the Arctic sea ice, turbulence exchanges heat between warm and cold air-mass by cooling (heating) warmer (colder) air (Figure 13h), simultaneously inducing a gradually thickening well-mixed layer capped by a strong inversion, and a continuously lifting of h_t and h_{sp} (Figure 13b). In this category, the well-mixed layer is substantially thinner than in category RAD, since the turbulent mixing here is mainly forced by surface friction, weaker and less effective than the buoyant mixing in category RAD (Figure 12b). Turbulence is mainly forced by wind shear and buoyancy, but buoyancy is negative here in the initially very stable near-surface layer. Therefore, wind shear mostly fuels the turbulent mixing. In category TBL, turbulent mixing is stronger than in category RAD, but the surface fluxes are still stronger, due to the stronger gradients; F_{sh} and F_{lh} are 77% and 42% larger than those in category RAD. Also see Figure 15c.

3.3.4 Turbulence-dominated with cold dome (TCD)

40% of WaMAIs over the Barents Sea belong to this category. For this category, the boundary-layer energy-budget is generally similar to that in category TBL. The main difference is that there is always a layer of cold air (cold dome) laying below the warm-and-moist air-mass especially in the central Arctic (Figure 14c). This cold dome enlarges the vertical temperature gradient and hence intensifies turbulent heat near the surface (Figure 14h). As the warm-and-moist air-mass is advected over the cold dome, it is gradually lifted up by the cold dome and consequently, h_t and h_{sp} are increasing at a faster rate than in category TBL (Figure 16b3). With faster lifting h_t and h_{sp}, F_{sh} and F_{lh} would be reduced more rapidly or even become negative in the high Arctic (Figure 16a3). TWP is dominated by LWP in category RAD and TWP is contributed almost equally by LWP and IWP in category TBL, while in category TCD, TWP is gradually more dominated by IWP; the IWP-to-TWP ratio increases linearly from ~50% to ~100% (Figure 16c3); also see Figure 15d.

4. Conclusion

Warm Arctic in winter is always related with long-lived blocking (Luo et al., 2017b, 2018). To the west of these blocks, Warm-and-moist air is transported to the Arctic, greatly contributing to Arctic surface warming. In this research, we name these warm events as warm-and-moist air intrusions (WaMAIs).As the persistence of Arctic blocking increases (Luo et al., 2017b), WaMAIs could be more frequent and hence lead to more amplified Arctic warming in winter (You et al., 2022). To understand the surface and boundary-layer energy-budget as WaMAIs occur, in this paper, we have detected WaMAIs over the Arctic Ocean sectors of Barents, Kara, Laptev, East Siberian, Chukchi and Beaufort Seas in 40 recent winters (DJF from 1979 to 2018) using ERA5 reanalysis. The climatological analysis shows a consistent pattern with a blocking high-pressure system over corresponding ocean sectors leads to warm-and-moist air intrusions into winter Arctic, supplying moisture for cloud formation, exerting a positive total energy-budget anomaly on the surface.

370   Statistically, as warm-and-moist air is advected over ocean sectors with land-locked ice cover, such as

371 the Laptev, East Siberian, Chukchi and Beaufort Seas, the longwave irradiance anomaly increases linearly by 2.5

372 $W\ m^{-2}$ (degree latitude)$^{-1}$, while the total column cloud liquid water increases linearly by 6 $g\ m^{-2}$ (degree latitude)$^{-}$

373 ^{1}. The longwave irradiance is dominant in the surface energy-budget. We have also analysed the boundary-layer

374 vertical structure along these trajectories, as well as the associated surface energy-budget pattern of over these

375 sectors, and find one main category, elevated lifting temperature inversion (INV), which in structure is similar to

376 summer WaMAIs (You et al., 2021) (Figure 15a).

377   During WaMAIs over the Barents Sea where open water exists to the south of the sea ice edge, turbulent

378 heat flux is dominant over the surface energy-budget, especially along the first half-way of the trajectories (Figure

379 10c). This difference on the surface energy-budget between the Barents Sea and frozen sea sectors is also

380 preliminarily discussed by Lee et al. (2017). Three main categories are found; radiation-dominated (category

381 RAD), turbulence-dominated (category TBL) and turbulent-dominated with cold dome (category TCD),

382 comprising 8%, 52% and 40%, respectively, of all WaMAIs. Unlike over the sectors with land-locked sea ice, air-

383 masses over the ice-free Barents Sea are warmed by the sea surface (local process) before being advected over

384 the sea ice (remote process), consequently resulting in more intensive surface warming.

385   In response to ten times smaller large-scale subsidence, stratocumulus develops more strongly in

386 category RAD with more intensive cloud-top radiative cooling, inducing apparently thicker well-mixed layer

387 (Figure 15b). However, this strong radiative cooling induces intensive buoyant mixing extending from the cloud

388 top till the surface, supresses the surface turbulent mixing and decreases the lifting rate of the height to the

389 maximum temperature (h_t) and to the maximum specific humidity (h_{sp}). Therefore, surface turbulent fluxes in

390 category RAD and the lifting rate of h_t and h_{sp} are apparently smaller than those in category TBL (Figure 15c).

391 With cold dome, less liquid cloud water could be formed and fewer or even negative turbulent fluxes could access

392 to the surface, in comparison with category TBL (Figure 15d). In category TCD, turbulent fluxes decrease faster

393 along the trajectory since warm-and-moist air is lifted to higher altitude above the cold dome (Figure 15d).

394   Under the background of global warming, the rate of local process has been accelerated by 9% per year

395 (Kim et al., 2019), while the meridional heat and moisture transports (remote processes) over the Barents Sea are

396 also enhanced in recent decades (Nygård et al., 2020). This implies that WaMAI may play a more significant role

397 in the future Arctic warming. Therefore, the potential mechanism which enhances the occurrence and intensity of

398 WaMAI deserves more attentions from atmospheric scientists.

399 **Data availability**

400 All data used can be found on the ERA5 data repository at DOI: www.ecmwf.int/en/forecasts/datasets/reanalysis-

401 datasets/era5.

402 **Author contributions**

403 CY conducted analysis and interpretation of the data under the supervision of MT and AD. CY prepared the

404 original version of the paper. MT and AD provided constructive comments and revisions to the final article.

405 **Competing interests**

406   The authors declare that they have no conflict of interest.

407   **Acknowledgements:**

408   This research was supported by the Swedish Research Council under Grant 2016-03807. The authors are grateful

409   to Cian Woods for providing the trajectory calculation algorithm.

410

411

References

Ali, S. M. and Pithan, F.: Following moist intrusions into the Arctic using SHEBA observations in a Lagrangian perspective, Q. J. R. Meteorol. Soc., 146(732), 3522–3533, doi:10.1002/qj.3859, 2020.

Andreas, E. L., Guest, P. S., Persson, P. O. G., Fairall, C. W., Horst, T. W., Moritz, R. E. and Semmer, S. R.: Near-surface water vapor over polar sea ice is always near ice saturation, J. Geophys. Res. Ocean., 107(10), doi:10.1029/2000jc000411, 2002.

Brooks, I. M., Tjernström, M., Persson, P. O. G., Shupe, M. D., Atkinson, R. A., Canut, G., Birch, C. E., Mauritsen, T., Sedlar, J. and Brooks, B. J.: The Turbulent Structure of the Arctic Summer Boundary Layer During The Arctic Summer Cloud-Ocean Study, J. Geophys. Res. Atmos., 122(18), 9685–9704, doi:10.1002/2017JD027234, 2017.

Cohen, J., Screen, J. A., Furtado, J. C., Barlow, M., Whittleston, D., Coumou, D., Francis, J., Dethloff, K., Entekhabi, D., Overland, J. and Jones, J.: Recent Arctic amplification and extreme mid-latitude weather, Nat. Geosci., 7(9), 627–637, doi:10.1038/ngeo2234, 2014.

Cox, C. J., Stone, R. S., Douglas, D. C., Stanitski, D. M. and Gallagher, M. R.: The Aleutian Low-Beaufort Sea Anticyclone: A Climate Index Correlated With the Timing of Springtime Melt in the Pacific Arctic Cryosphere, Geophys. Res. Lett., 46(13), 7464–7473, doi:10.1029/2019GL083306, 2019.

Draxler, R. R.: Sensitivity of a Trajectory Model to the Spatial and Temporal Resolution of the Meteorological Data during CAPTEX, J. Clim. Appl. Meteorol., 26(11), 1577–1588, doi:10.1175/1520-0450(1987)026<1577:soatmt>2.0.co;2, 1987.

Gong, T. and Luo, D.: Ural blocking as an amplifier of the Arctic sea ice decline in winter, J. Clim., 30(7), 2639–2654, doi:10.1175/JCLI-D-16-0548.1, 2017.

Gong, T., Feldstein, S. and Lee, S.: The role of downward infrared radiation in the recent arctic winter warming trend, J. Clim., 30(13), 4937–4949, doi:10.1175/JCLI-D-16-0180.1, 2017.

Graham, R. M., Cohen, L., Ritzhaupt, N., Segger, B., Graversen, R. G., Rinke, A., Walden, V. P., Granskog, M. A. and Hudson, S. R.: Evaluation of six atmospheric reanalyses over Arctic sea ice from winter to early summer, J. Clim., 32(14), 4121–4143, doi:10.1175/JCLI-D-18-0643.1, 2019.

Graversen, R. G., Mauritsen, T., Tjernström, M., Källén, E. and Svensson, G.: Vertical structure of recent Arctic warming, Nature, 451(7174), 53–56, doi:10.1038/nature06502, 2008a.

Graversen, R. G., Mauritsen, T., Tjernström, M., Källén, E. and Svensson, G.: Vertical structure of recent Arctic warming, Nature, 451(7174), 53–56, doi:10.1038/nature06502, 2008b.

Hersbach, H., Bell, B., Berrisford, P., Hirahara, S., Horányi, A., Muñoz-Sabater, J., Nicolas, J., Peubey, C., Radu, R., Schepers, D., Simmons, A., Soci, C., Abdalla, S., Abellan, X., Balsamo, G., Bechtold, P., Biavati, G., Bidlot, J., Bonavita, M., De Chiara, G., Dahlgren, P., Dee, D., Diamantakis, M., Dragani, R., Flemming, J., Forbes, R., Fuentes, M., Geer, A., Haimberger, L., Healy, S., Hogan, R. J., Hólm, E., Janisková, M., Keeley, S., Laloyaux, P., Lopez, P., Lupu, C., Radnoti, G., de Rosnay, P., Rozum, I., Vamborg, F., Villaume, S. and

447   Thépaut, J. N.: The ERA5 global reanalysis, Q. J. R. Meteorol. Soc., 146(730), 1999–2049,

448   doi:10.1002/qj.3803, 2020.

449   Kim, B. -M., Son, S. -W., Min, S. -K., Jeong, J. -H., Kim, S. -J., Zhang, X., Shim, T. and Yoon, J. -H.:

450   Weakening of the stratospheric polar vortex by Arctic sea-ice loss, Nat. Commun., 5, doi:10.1038/ncomms5646,

451   2014.

452   Kim, K. -Y. and Son, S. -W.: Physical characteristics of Eurasian winter temperature variability, Environ. Res.

453   Lett., 11(4), doi:10.1088/1748-9326/11/4/044009, 2016.

454   Kim, K. -Y., Kim, J. -Y., Kim, J., Yeo, S., Na, H., Hamlington, B. D. and Leben, R. R.: Vertical Feedback

455   Mechanism of Winter Arctic Amplification and Sea Ice Loss, Sci. Rep., doi:10.1038/s41598-018-38109-x,

456   2019.

457   Komatsu, K. K., Alexeev, V. A., Repina, I. A. and Tachibana, Y.: Poleward upgliding Siberian atmospheric

458   rivers over sea ice heat up Arctic upper air, Sci. Rep., 8(1), doi:10.1038/s41598-018-21159-6, 2018.

459   Lee, S., Gong, T., Feldstein, S. B., Screen, J. A. and Simmonds, I.: Revisiting the Cause of the 1989–2009

460   Arctic Surface Warming Using the Surface Energy Budget: Downward Infrared Radiation Dominates the

461   Surface Fluxes, Geophys. Res. Lett., 44(20), 10,654-10,661, doi:10.1002/2017GL075375, 2017.

462   Li, M., Luo, D., Simmonds, I., Dai, A., Zhong, L. and Yao, Y.: Anchoring of atmospheric teleconnection

463   patterns by Arctic Sea ice loss and its link to winter cold anomalies in East Asia, Int. J. Climatol., 41(1), 547–

464   558, doi:10.1002/joc.6637, 2021.

465   Lindsay, R., Wensnahan, M., Schweiger, A. and Zhang, J.: Evaluation of seven different atmospheric reanalysis

466   products in the arctic, J. Clim., 27(7), 2588–2606, doi:10.1175/JCLI-D-13-00014.1, 2014.

467   Liu, Y., Key, J. R., Vavrus, S. and Woods, C.: Time evolution of the cloud response to moisture intrusions into

468   the Arctic during Winter, J. Clim., 31(22), 9389–9405, doi:10.1175/JCLI-D-17-0896.1, 2018.

469   Luo, B., Luo, D., Wu, L., Zhong, L. and Simmonds, I.: Atmospheric circulation patterns which promote winter

470   Arctic sea ice decline, Environ. Res. Lett., 12(5), doi:10.1088/1748-9326/aa69d0, 2017a.

471   Luo, D., Yao, Y., Dai, A., Simmonds, I. and Zhong, L.: Increased quasi stationarity and persistence of winter

472   ural blocking and Eurasian extreme cold events in response to arctic warming. Part II: A theoretical explanation,

473   J. Clim., 30(10), 3569–3587, doi:10.1175/JCLI-D-16-0262.1, 2017b.

474   Luo, D., Chen, X., Dai, A. and Simmonds, I.: Changes in atmospheric blocking circulations linked with winter

475   Arctic warming: A new perspective, J. Clim., 31(18), 7661–7678, doi:10.1175/JCLI-D-18-0040.1, 2018.

476   Luo, D., Chen, X., Overland, J., Simmonds, I., Wu, Y. and Zhang, P.: Weakened potential vorticity barrier

477   linked to recent winter Arctic Sea ice loss and midlatitude cold extremes, J. Clim., 32(14), 4235–4261,

478   doi:10.1175/JCLI-D-18-0449.1, 2019.

479   Mayer, M., Tietsche, S., Haimberger, L., Tsubouchi, T., Mayer, J. and Zuo, H. A. O.: An improved estimate of

480   the coupled Arctic energy budget, J. Clim., 32(22), 7915–7934, doi:10.1175/JCLI-D-19-0233.1, 2019.

481 Messori, G., Woods, C. and Caballero, R.: On the drivers of wintertime temperature extremes in the high arctic,
482 J. Clim., 31(4), 1597–1618, doi:10.1175/JCLI-D-17-0386.1, 2018.

483 Mori, M., Watanabe, M., Shiogama, H., Inoue, J. and Kimoto, M.: Robust Arctic sea-ice influence on the
484 frequent Eurasian cold winters in past decades, Nat. Geosci., 7(12), 869–873, doi:10.1038/ngeo2277, 2014.

485 Morrison, H., De Boer, G., Feingold, G., Harrington, J., Shupe, M. D. and Sulia, K.: Resilience of persistent
486 Arctic mixed-phase clouds, Nat. Geosci., 5(1), 11–17, doi:10.1038/ngeo1332, 2012.

487 Nygård, T., Naakka, T. and Vihma, T.: Horizontal moisture transport dominates the regional moistening patterns
488 in the arctic, J. Clim., 33(16), 6793–6807, doi:10.1175/JCLI-D-19-0891.1, 2020.

489 Overland, J. E. and Wang, M.: Recent extreme arctic temperatures are due to a split polar vortex, J. Clim.,
490 29(15), 5609–5616, doi:10.1175/JCLI-D-16-0320.1, 2016.

491 Overland, J. E., Wood, K. R. and Wang, M.: Warm Arctic-cold continents: Climate impacts of the newly open
492 arctic sea, Polar Res., doi:10.3402/polar.v30i0.15787, 2011.

493 Papritz, L.: Arctic lower-tropospheric warm and cold extremes: Horizontal and vertical transport, diabatic
494 processes, and linkage to synoptic circulation features, J. Clim., 33(3), 993–1016, doi:10.1175/JCLI-D-19-
495 0638.1, 2020.

496 Papritz, L., Hauswirth, D. and Hartmuth, K.: Moisture origin, transport pathways, and driving processes of
497 intense wintertime moisture transport into the Arctic, Weather Clim. Dyn., 3(1), 1–20, doi:10.5194/wcd-3-1-
498 2022, 2022.

499 Persson, P. O. G., Fairall, C. W., Andreas, E. L., Guest, P. S. and Perovich, D. K.: Measurements near the
500 Atmospheric Surface Flux Group tower at SHEBA: Near-surface conditions and surface energy budget, J.
501 Geophys. Res. Ocean., 107(10), doi:10.1029/2000jc000705, 2002.

502 Petoukhov, V. and Semenov, V. A.: A link between reduced Barents-Kara sea ice and cold winter extremes over
503 northern continents, J. Geophys. Res. Atmos., doi:10.1029/2009JD013568, 2010.

504 Pithan, F., Medeiros, B. and Mauritsen, T.: Mixed-phase clouds cause climate model biases in Arctic wintertime
505 temperature inversions, Clim. Dyn., 43(1–2), 289–303, doi:10.1007/s00382-013-1964-9, 2014.

506 Pithan, F., Svensson, G., Caballero, R., Chechin, D., Cronin, T. W., Ekman, A. M. L., Neggers, R., Shupe, M.
507 D., Solomon, A., Tjernström, M. and Wendisch, M.: Role of air-mass transformations in exchange between the
508 Arctic and mid-latitudes, Nat. Geosci., 11(11), 805–812, doi:10.1038/s41561-018-0234-1, 2018.

509 Rudeva, I. and Simmonds, I.: Midlatitude winter extreme temperature events and connections with anomalies in
510 the arctic and tropics, J. Clim., 34(10), 3733–3749, doi:10.1175/JCLI-D-20-0371.1, 2021.

511 Screen, J. A. and Simmonds, I.: The central role of diminishing sea ice in recent Arctic temperature
512 amplification, Nature, 464(7293), 1334–1337, doi:10.1038/nature09051, 2010.

513 Screen, J. A., Bracegirdle, T. J. and Simmonds, I.: Polar Climate Change as Manifest in Atmospheric
514 Circulation, Curr. Clim. Chang. Reports, 4(4), 383–395, doi:10.1007/s40641-018-0111-4, 2018.

515 Sedlar, J. and Tjernström, M.: Clouds, warm air, and a climate cooling signal over the summer Arctic, Geophys.
516 Res. Lett., 44(2), 1095–1103, doi:10.1002/2016GL071959, 2017.

517 Serreze, M. C. and Francis, J. A.: The arctic amplification debate, Clim. Change, 76(3–4), 241–264,
518 doi:10.1007/s10584-005-9017-y, 2006.

519 Simmonds, I.: Comparing and contrasting the behaviour of Arctic and Antarctic sea ice over the 35 year period
520 1979-2013, Ann. Glaciol., 56(69), 18–28, doi:10.3189/2015AoG69A909, 2015.

521 Simmonds, I. and Li, M.: Trends and variability in polar sea ice, global atmospheric circulations, and
522 baroclinicity, Ann. N. Y. Acad. Sci., 1504(1), 167–186, doi:10.1111/nyas.14673, 2021.

523 Sotiropoulou, G., Sedlar, J., Tjernström, M., Shupe, M. D., Brooks, I. M. and Persson, P. O. G.: The
524 thermodynamic structure of summer Arctic stratocumulus and the dynamic coupling to the surface, Atmos.
525 Chem. Phys., 14(22), 12573–12592, doi:10.5194/acp-14-12573-2014, 2014.

526 Stohl, A., Wotawa, G., Seibert, P. and Kromp-Kolb, H.: Interpolation errors in wind fields as a function of
527 spatial and temporal resolution and their impact on different types of kinematic trajectories, J. Appl. Meteorol.,
528 34(10), 2149–2165, doi:10.1175/1520-0450(1995)034<2149:IEIWFA>2.0.CO;2, 1995.

529 Tang, Q., Zhang, X., Yang, X. and Francis, J. A.: Cold winter extremes in northern continents linked to Arctic
530 sea ice loss, Environ. Res. Lett., doi:10.1088/1748-9326/8/1/014036, 2013.

531 Tjernström, M. and Graversen, R. G.: The vertical structure of the lower Arctic troposphere analysed from
532 observati0ns and the ERA-40 reanalysis, Q. J. R. Meteorol. Soc., 135(639), 431–443, doi:10.1002/qj.380, 2009.

533 Tjernström, M., Birch, C. E., Brooks, I. M., Shupe, M. D., Persson, P. O. G., Sedlar, J., Mauritsen, T., Leck, C.,
534 Paatero, J., Szczodrak, M. and Wheeler, C. R.: Meteorological conditions in the central Arctic summer during
535 the Arctic Summer Cloud Ocean Study (ASCOS), Atmos. Chem. Phys., 12(15), 6863–6889, doi:10.5194/acp-
536 12-6863-2012, 2012.

537 Tjernström, M., Shupe, M. D., Brooks, I. M., Persson, P. O. G., Prytherch, J., Salisbury, D. J., Sedlar, J.,
538 Achtert, P., Brooks, B. J., Johnston, P. E., Sotiropoulou, G. and Wolfe, D.: Warm-air advection, air mass
539 transformation and fog causes rapid ice melt, Geophys. Res. Lett., 42(13), 5594–5602,
540 doi:10.1002/2015GL064373, 2015.

541 Tjernström, M., Shupe, M. D., Brooks, I. M., Achtert, P., Prytherch, J. and Sedlar, J.: Arctic summer airmass
542 transformation, surface inversions, and the surface energy budget, J. Clim., 32(3), 769–789, doi:10.1175/JCLI-
543 D-18-0216.1, 2019.

544 Wang, C., Graham, R. M., Wang, K., Gerland, S. and Granskog, M. A.: Comparison of ERA5 and ERA-Interim
545 near-surface air temperature, snowfall and precipitation over Arctic sea ice: effects on sea ice thermodynamics
546 and evolution, Cryosphere, 13(6), 1661–1679, doi:10.5194/tc-13-1661-2019, 2019.

547 Woods, C. and Caballero, R.: The role of moist intrusions in winter arctic warming and sea ice decline, J. Clim.,
548 29(12), 4473–4485, doi:10.1175/JCLI-D-15-0773.1, 2016.

549   Woods, C., Caballero, R. and Svensson, G.: Large-scale circulation associated with moisture intrusions into the

550   Arctic during winter, Geophys. Res. Lett., 40(17), 4717–4721, doi:10.1002/grl.50912, 2013.

551   You, C., Tjernström, M. and Devasthale, A.: Warm-Air Advection Over Melting Sea-Ice: A Lagrangian Case

552   Study, Boundary-Layer Meteorol., doi:10.1007/s10546-020-00590-1, 2020.

553   You, C., Tjernström, M. and Devasthale, A.: Eulerian and Lagrangian views of warm and moist air intrusions

554   into summer Arctic, Atmos. Res., 256, doi:10.1016/j.atmosres.2021.105586, 2021.

555   You, C., Tjernström, M., Devasthale, A. and Steinfeld, D.: The role of atmospheric blocking in regulating Arctic

556   warming, Geophys. Res. Lett, 2022. (under review)

557

558

559

Table 1. Regional averaged F_{sh}, F_{lh}, F_{sw}, F_{lw} and F_{total} in Kara, Laptev, East Siberian and Beaufort Sea sector. The unit is W m^{-2} for all variables. Statistically significant positive values are in bold.

Sea sector	Barents	Kara	Laptev	East Siberian	Chukchi	Beaufort
F_{sh}	**28.85±16.73**	8.92±13.08	3.17±6.53	6.72±7.77	**13.55±10.87**	5.93 ±8.14
F_{lh}	**10.05±9.83**	0.65±6.58	-0.39±2.19	0.55±2.56	1.56±4.02	0.34±2.19
F_{sw}	-0.024±0.59	-0.077±0.40	-0.029±0.40	-0.16±0.47	-0.095±0.97	-0.077±0.9
F_{lw}	**15.99±14.34**	**16.51±9.93**	5.92±10.88	**15.42±11.16**	**21.77±10.30**	**17.45±10.51**
F_{total}	**54.86±34.41**	**26.01±25.32**	8.67±13.81	**22.52±15.08**	**36.78±16.27**	**23.65±14.85**

Table 2. Number of WaMAIs with boundary layer energy budget pattern of category RAD (radiation-dominated), TBL (turbulence-dominated), TCD (turbulence-dominated with cold dome) and INV (lifting temperature inversion), over melting (Barents) and frozen (Laptev, East Siberian, Chukchi and Beaufort) sea sectors.

Sea sector	Melting			Frozen
Category	RAD	TBL	TCD	INV
Number	9	45	33	131

Table 3. Averaged F_{sh}, F_{lh}, F_{sw}, F_{lw}, TCLW (from bottom to h_{t_z}; g m^{-2}) and large-scale convergence (CONV; 10^{-5} kg m^{-2} s^{-1}) from category TBL and category RAD. Statistically significant positive values are in bold.

	Category RAD	Category TBL	Category TCD
F_{sw}	-0.0094±0.047	-0.00035±0.0013	-0.0050±0.035
F_{lw}	**31.49±13.96**	**34.61±18.71**	**35.46±13.10**
F_{sh}	**40.99±28.27**	**72.58±40.21**	9.77±23.08
F_{lh}	**17.43±15.42**	**24.79±23.80**	1.02±8.16
TCLW	**96.78±53.31**	**83.11±54.27**	30.13±31.89
CONV	17.19±174.89	**236.05±225.90**	115.00±230.01
Wind Shear	**0.019±0.0061**	**0.026±0.008**	**0.02±0.011**
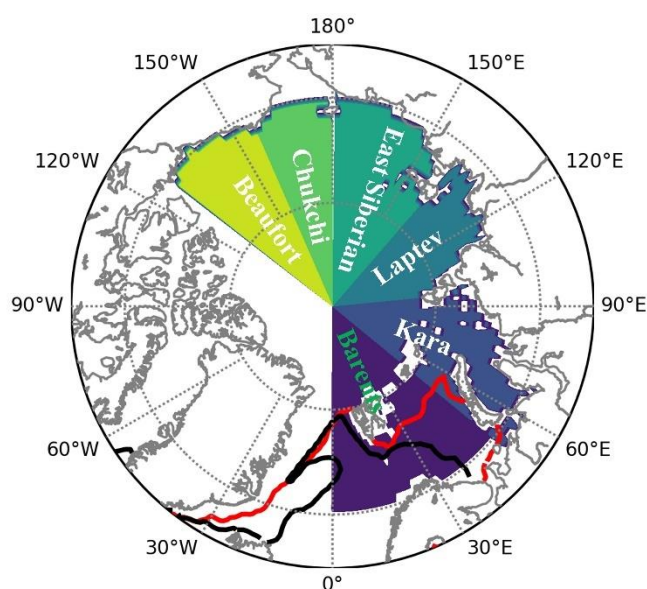
Figure 1. Locations of six sea sectors discussed in this paper, the Barents, Kara, Laptev, East Siberian, Chukchi and Beaufort Sea sectors. Black line is the mean March sea-ice edge in 1979 and red line is the mean March sea-ice edge in 2015 when the minimum winter sea ice cover was recorded.
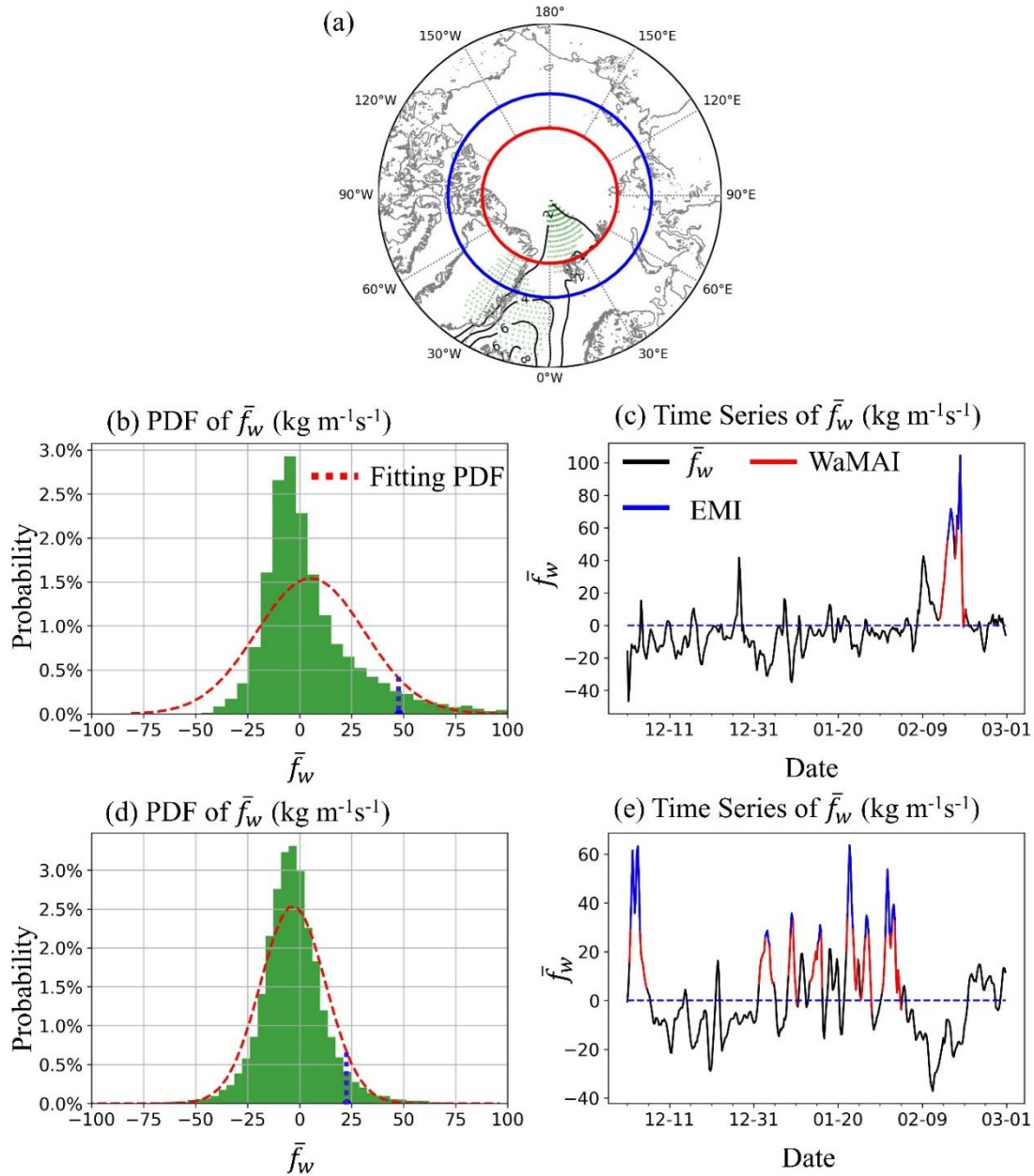
Figure 2. (a) Contours of the linear regrssion between local f_w and normalized SIC anomalies (multiplied by -1), defined as the anomaly divided by its standard deviation, for the winter months (DJF) over the Barents Sea. The stippling indicates statistical significance at the $p < 0.05$ level for the Student's t test. Note that the linear regression is calculated against standardized sea ice concentration. Therefore, its unit is same as the unit of f_w and the value represents the general variation of f_w from the climate mean during the sea ice retreat. Red line is the latitude of 80°N where the trajectories over the Barents Sea are launched, while blue line is the latitude of 75°N where the trajectories are launched over the sea sectors of Kara, Laptev, East Siberian, Chukchi and Beaufort; (b) and (d) show the Probability Distribution Function of $\bar{f}_w$ over the Barents and Beaufort Sea, respectively, with the 95-percentile marked as a blue

589 dashed line; (c) and (e) are the time series of $\bar{f}_w$ over the Barents Sea and Beaufort Sea in 1980,

590 respectively, with WaMAI highlighted in red and EMIs highlighted in blue.

591
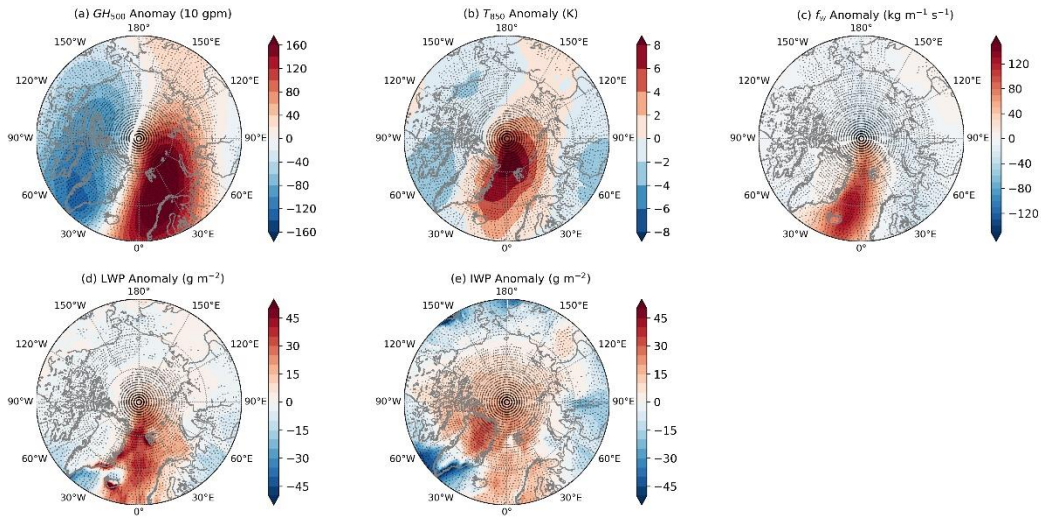
592 Figure 3. Composite ERA5 anomalies of (a) 500-hPa GH (10 gpm), (b) 850-hPa temperature
593 (K), (c) northward water-vapor flux ($kgm^{-1}s^{-1}$), (d) liquid water path (g m⁻²), and (e) ice
594 water path for all EMIs over the Barents Sea, during 1979~2018 winters. The stippling
595 indicates statistical significance at the $p < 0.01$ level from a Student's t test.

596

597

598
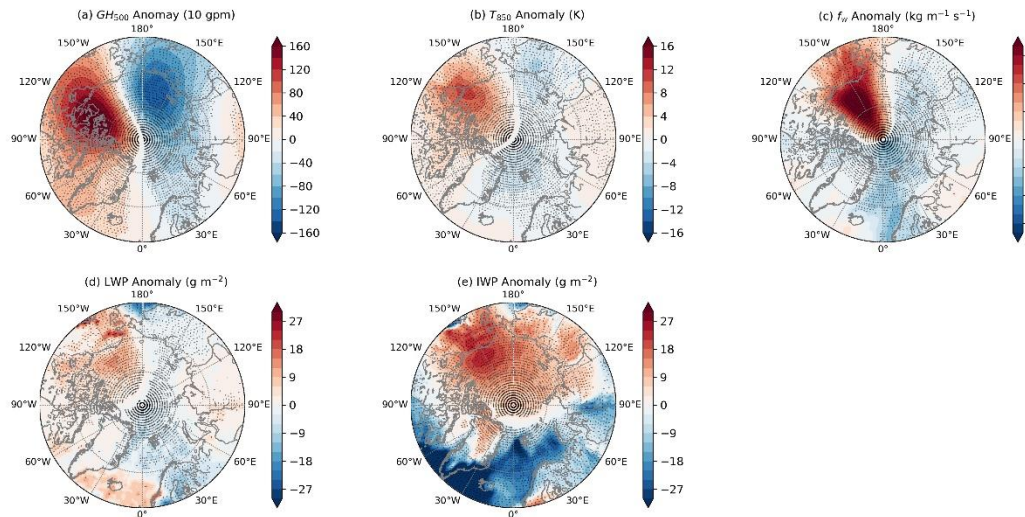
599 Figure 4. Composite ERA5 anomalies of (a) 500-hPa GH (10 gpm), (b) 850-hPa temperature
600 (K), (c) northward water-vapor flux ($kgm^{-1}s^{-1}$), (d) liquid water path (g m⁻²), and (e) ice
601 water path for all EMIs over the Beaufort Sea, during 1979~2018 winters. The stippling
602 indicates statistical significance at the $p < 0.01$ level from a Student's t test.

604

605

606
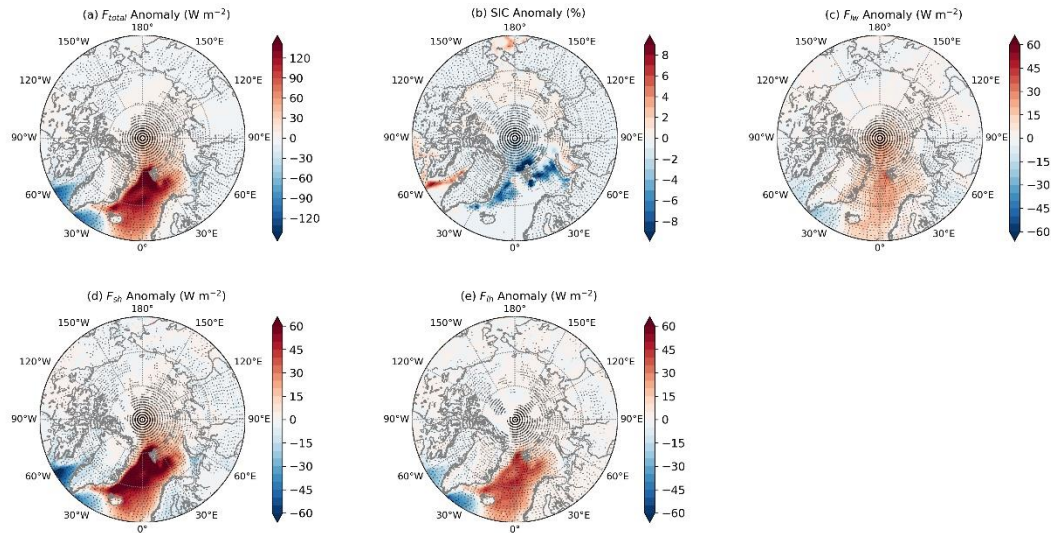
Figure 5. Composite ERA5 anomalies of (a) total surface energy (W m^{-2}), (b) sea ice concentration (%), (c) surface thermal net irradiance (W m^{-2}), (d) surface sensible heat flux (W m^{-2}) and (e) surface latent heat flux (W m^{-2}) for all EMIs over the Barents Sea, during 1979~2018 winter. The stippling indicates statistical significance at the $p < 0.01$ level from a Student's t test.

612
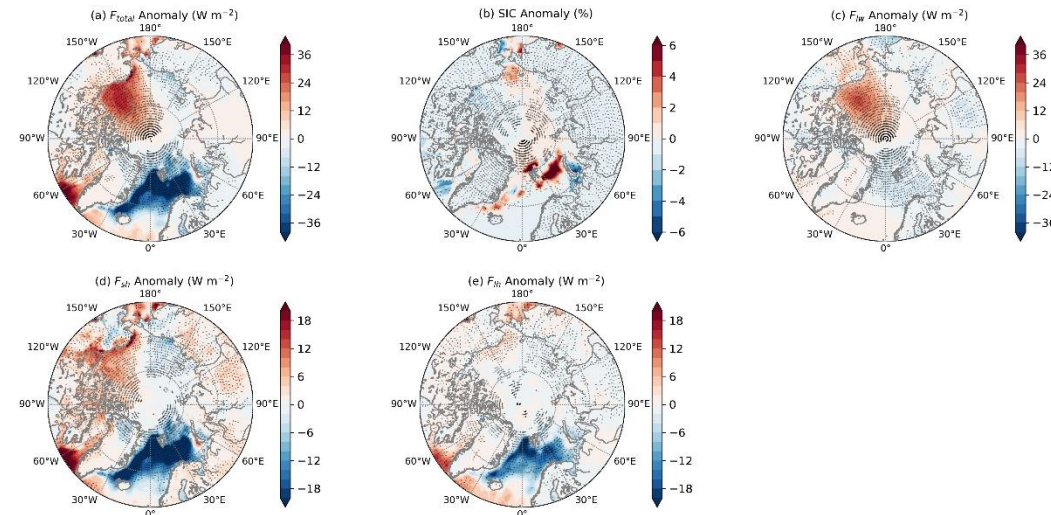
Figure 6. Composite ERA5 anomalies of (a) total surface energy (W m^{-2}), (b) sea ice concentration (%), (c) surface thermal net irradiance (W m^{-2}), (d) surface sensible heat flux (W m^{-2}) and (e) surface latent heat flux (W m^{-2}) for all EMIs over the Beaufort Sea, during 1979~2018 winter. Noted that the color-bars here are different than those in figure 5. The stippling indicates statistical significance at the $p < 0.01$ level from a Student's t test.

618
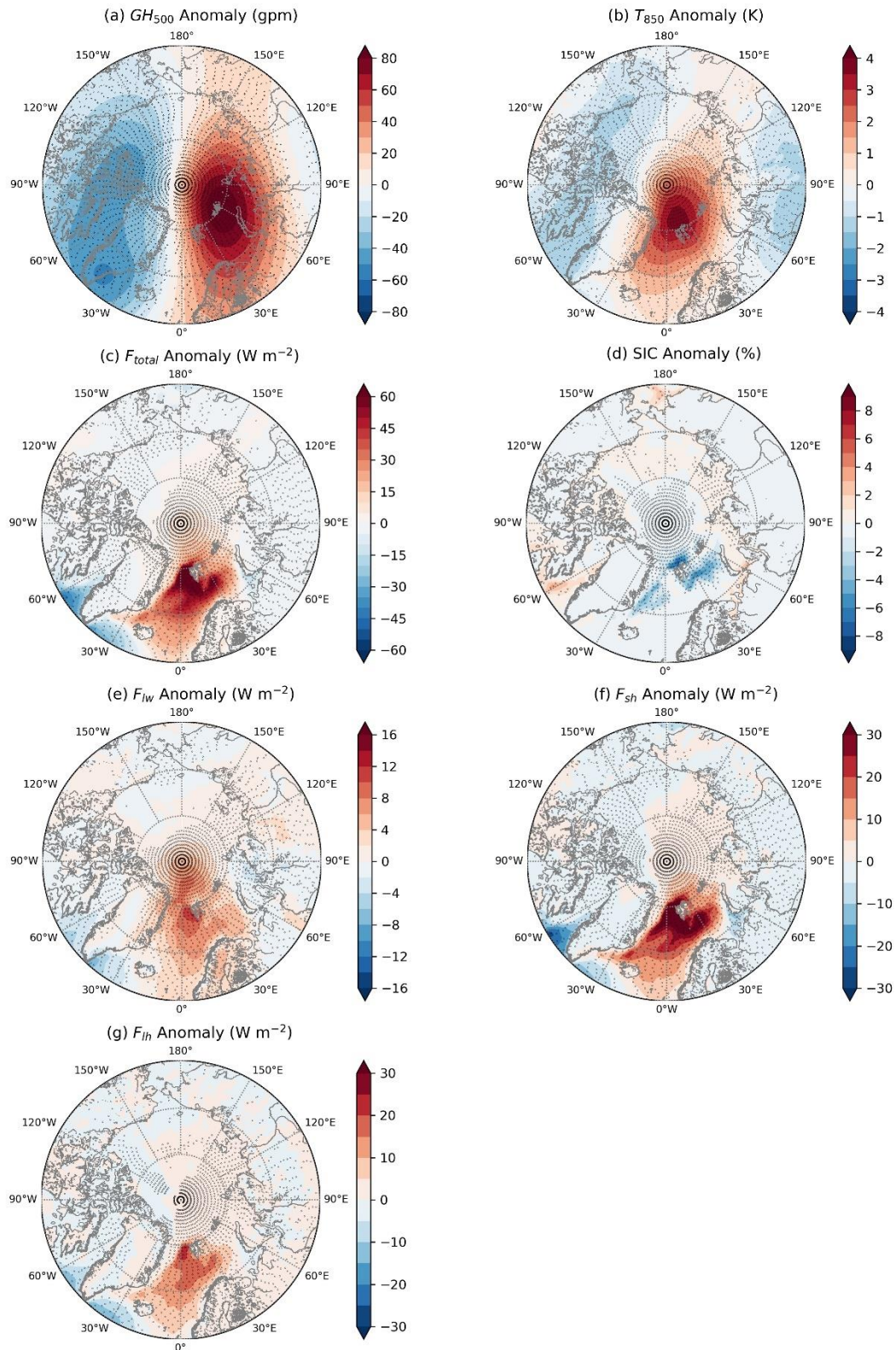
619
Figure 7. Anomalies of (a) 500-hPa geopotential height (gpm), (b) 850-hPa temperature (K),
(c) F_{total}, (d) SIC, (e) F_{lw}, (f) F_{sh}, and (g) F_{lh} from linear regressions against daily $\bar{f}_w$ time
series over the Barents Sea. The stippling indicates statistical significance at the $p < 0.05$ level
from a Student's t test.

624

625
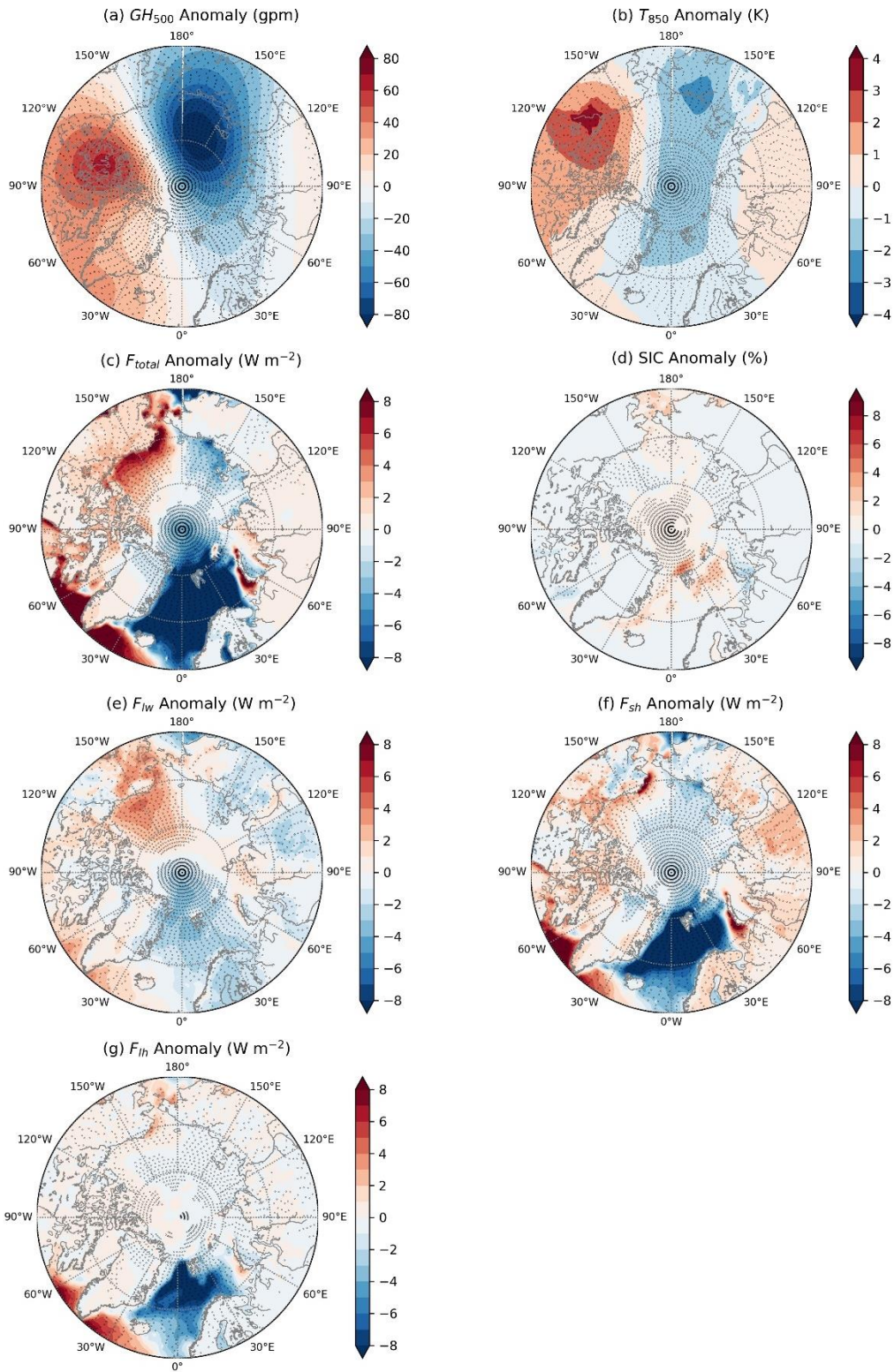
Figure 8. Anomalies of (a) 500-hPa geopotential height (gpm), (b) 850-hPa temperature (K), (c) F_{total}, (d) SIC, (e) F_{lw}, (f) F_{sh}, and (g) F_{lh} from linear regressions against daily $\bar{f}_w$ time series over the Beaufort Sea. The stippling indicates statistical significance at the $p < 0.05$ level from a Student's t test. Similar as figure 2a, the linear regressions here are calculated against standardized f_w. Therefore, the unit of the regression is same as the corresponding

626

627
628
629
630
631

632 variables and the values represent the general anomalies from the climate mean during

633 positive f_w.

634

635
636
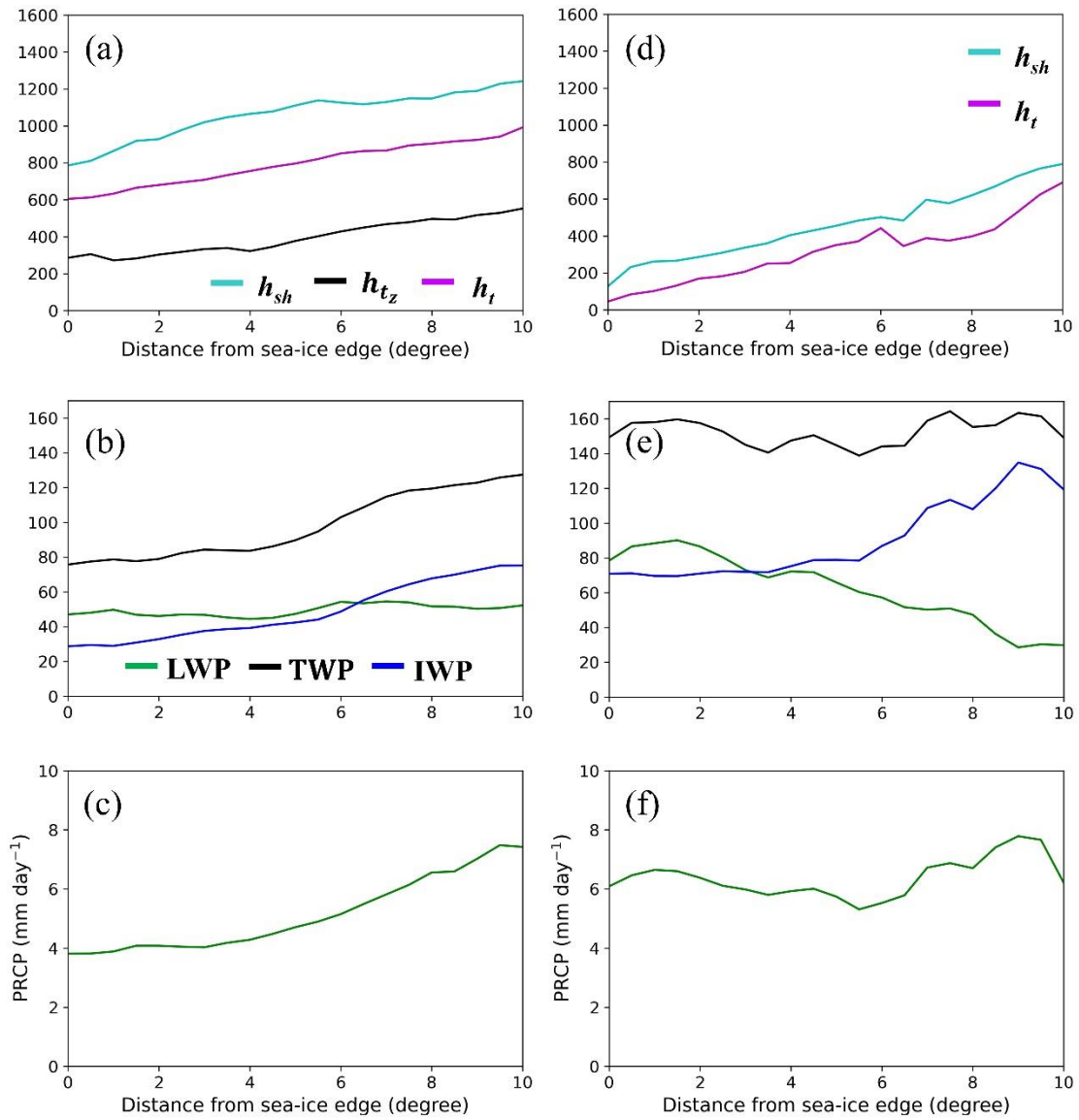
Figure 9: Average variation of (a) the height to the maximum specific humidity (h_{sh}),
temperature gradient (h_{t_z}; m) and temperature (h_t); (b) liquid water path (LWP; g m^{-2}), ice
water path (IWP; g m^{-2}) and total water path (TWP; g m^{-2}); (c) precipitation rate (PRCP; mm
day^{-1}), with the downstream northward distance from sea-ice edge, along the WaMAI
trajectories over the Barents Sea. (d) (e) (f) are the counterparts of (a)(b)(c) over the frozen
seas. Note that this is not necessarily the distance travelled, since WaMAIs do not need to travel
due northward.

644
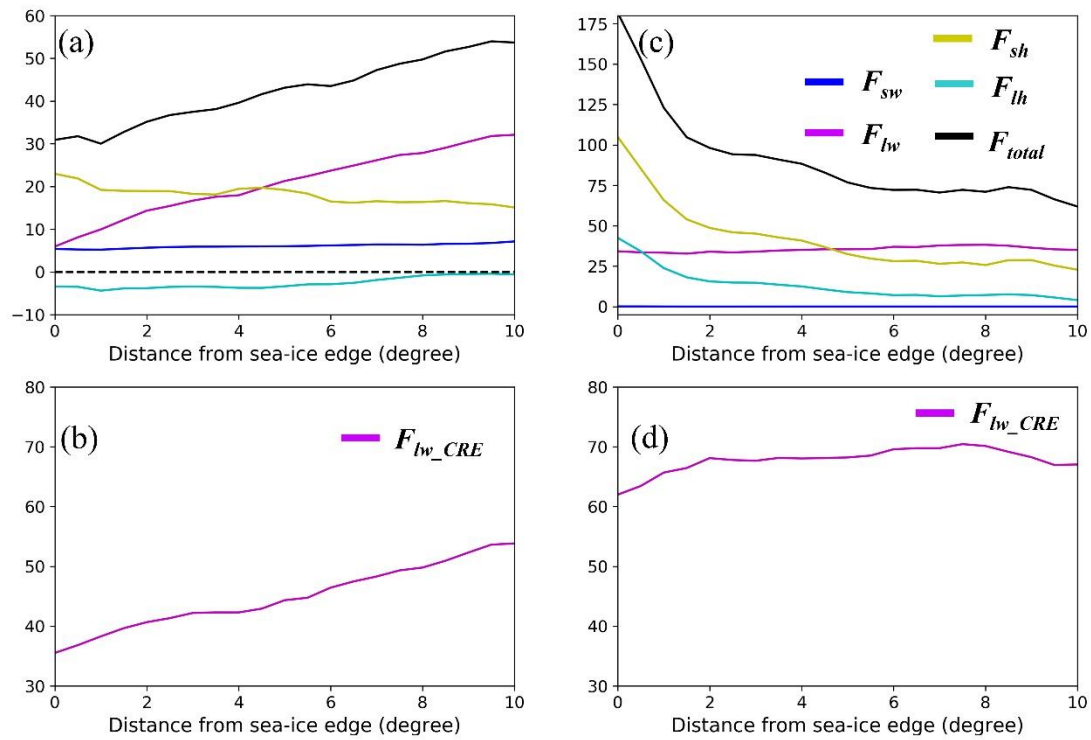
Figure 10. the average meridional evolution in the anomalies of (a) the sum (F_{total}, W m^{-2}; black) and individual surface fluxes of sensible heat (F_{sh}, W m^{-2}; yellow), latent heat (F_{lh}, W m^{-2}; cyan), net longwave irradiance (F_{lw}, W m^{-2}; magenta) and net shortwave irradiance (F_{sw}, W m^{-2}; blue) along the trajectories. (b) shows the cloud radiative effect by longwave (F_{lw_CRE}; magenta) over the Barents Sea. (c)(d) are the counterparts of (a)(b) over the frozen seas.

652

653
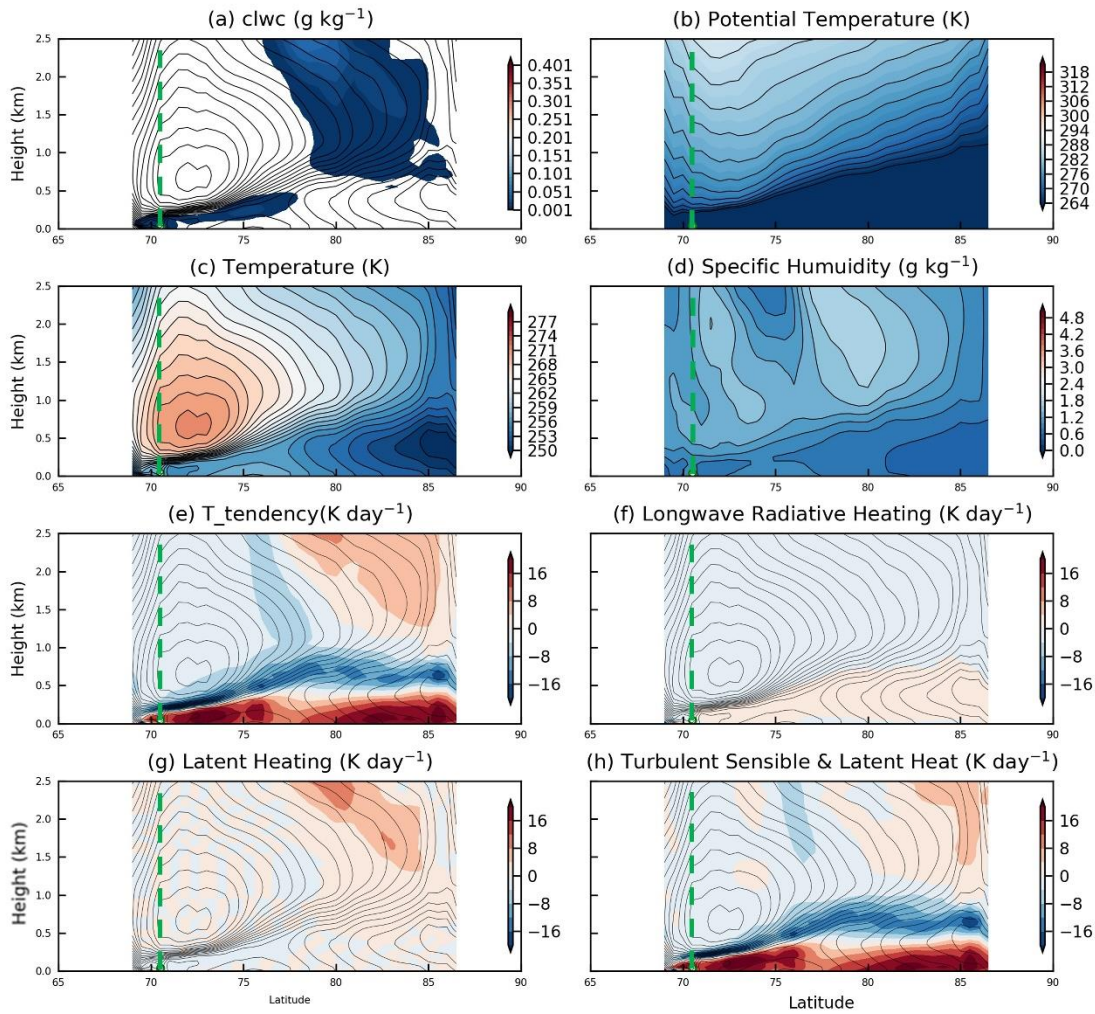
Figure 11. Latitude-height cross-section of (a) cloud liquid water concentration (g kg^{-1}), (b) potential temperature (K), (c) temperature (K), (d) specific humidity (g kg^{-1}), (e) temperature tendency due to model physics (K day^{-1}), (f) longwave radiative heating (K day^{-1}), (g) latent heating (K day^{-1}) and (h) turbulent heating (K day^{-1}), interpolated from ERA5 along trajectories of one selected WaMAI from category INV. The green dash lines mark the location of ice-edge. See the text for a detailed discussion.

660

661

662

663

664
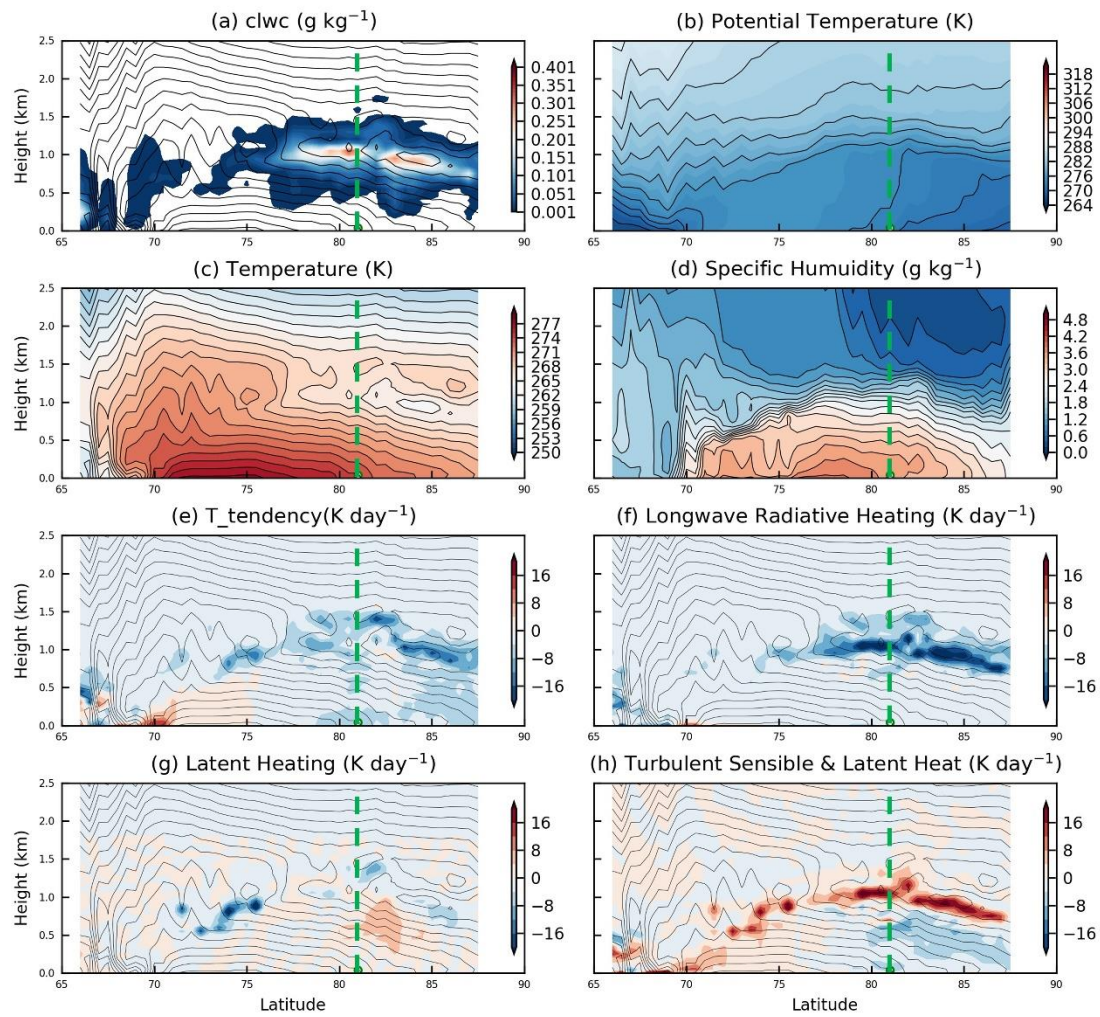
Figure 12. Same as figure 11 but for a selected radiation-dominated WaMAI.

666
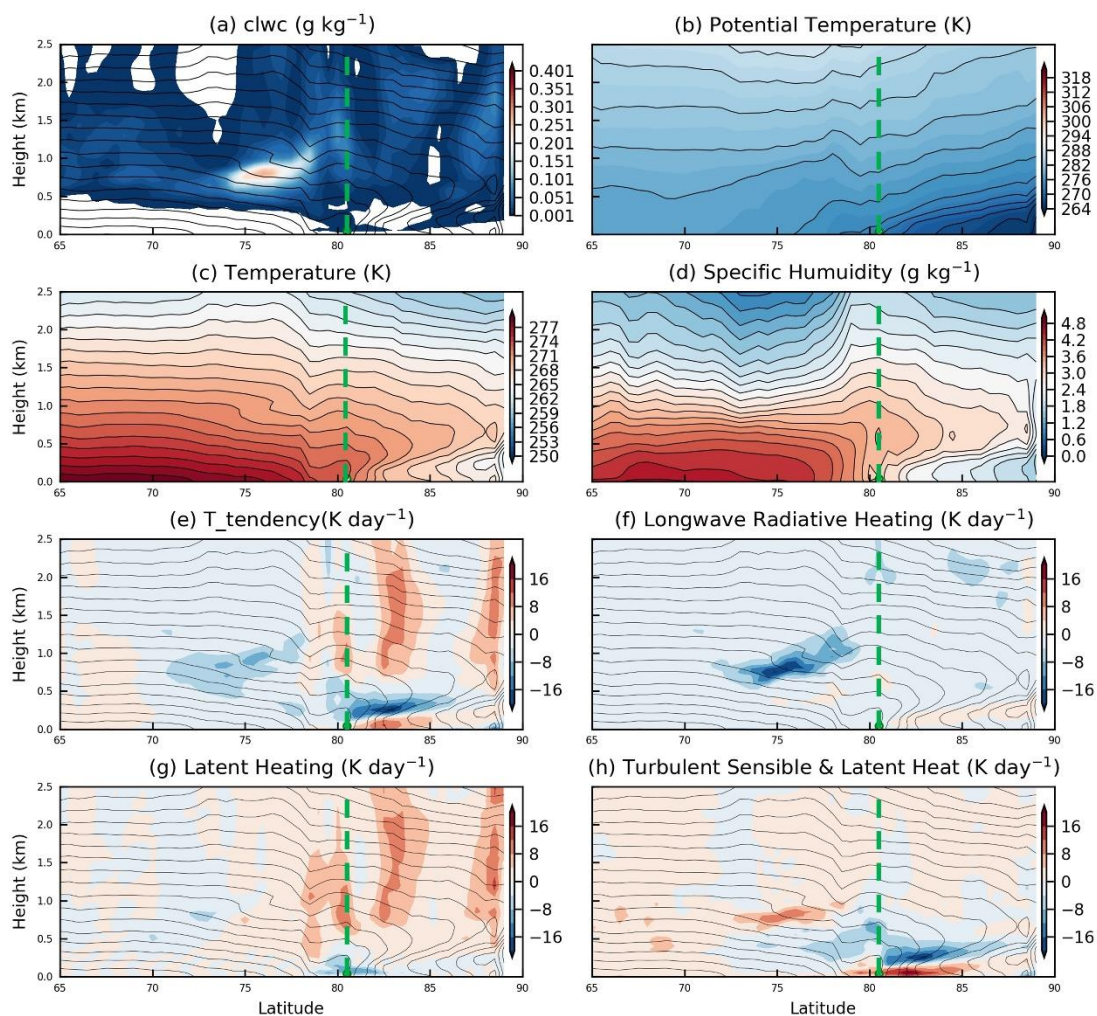
Figure 13. Same as figure 11 but for a selected turbulence-dominated WaMAI.

670
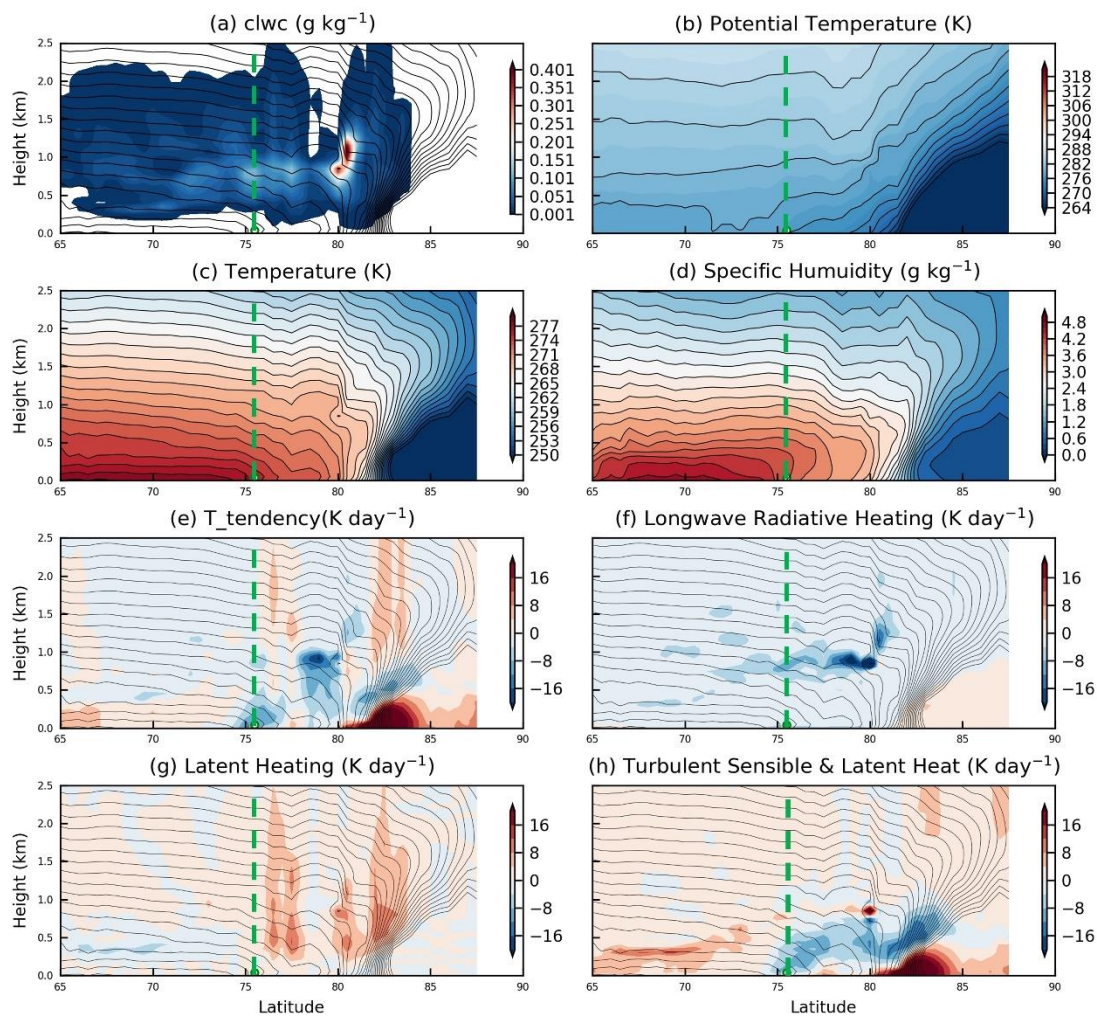
674   Figure 14. Same as figure 11 but for a selected turbulence-dominated WaMAI with cold
675   dome.
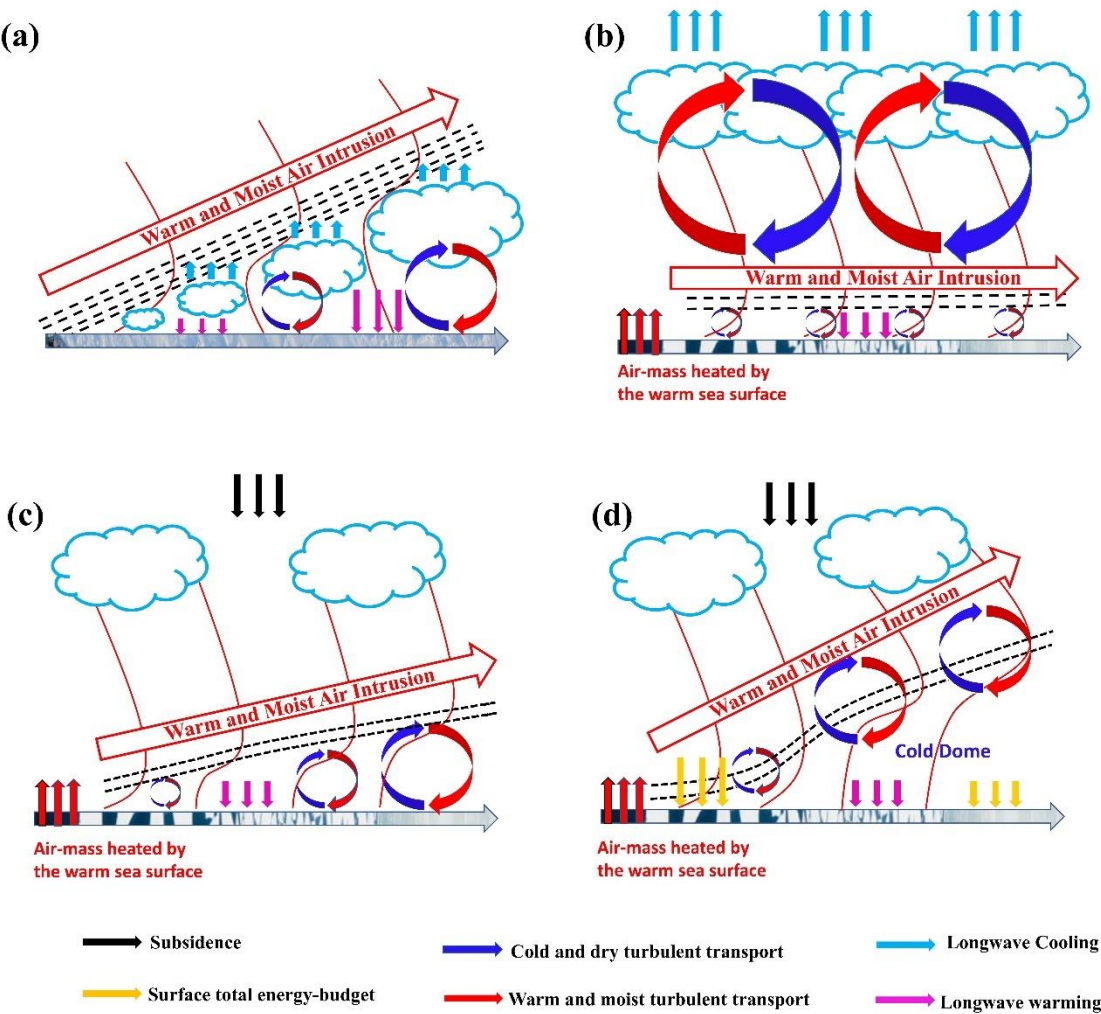
679 Figure 15. Concept graph of WaMAI from category (a) INV, (b) radiation-dominated
680 WaMAI, (c) turbulence-dominated WaMAI, (d) turbulence-dominated WaMAI with cold
681 dome. The red lines in (a)(b)(c) are temperature or humidity profiles. Red arrows represent
682 the WaMAIs. The horizontal arrows represent the Arctic surface with frozen or melting sea-
683 ice. Black lines represent inversions.

684

685
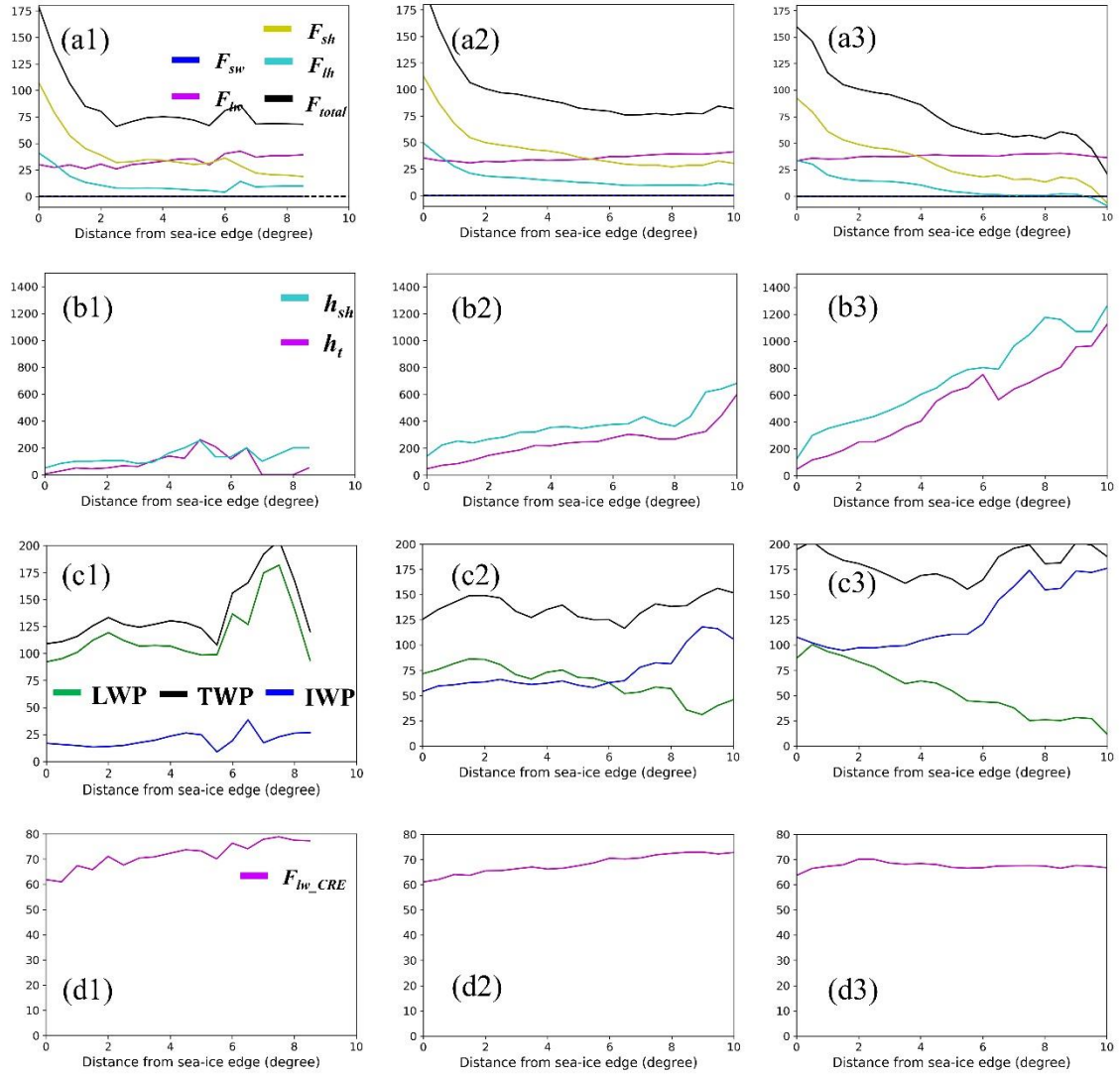
Figure 16. Average variation of (a1) the sum (F_{total}, W m^{-2}; black) and individual surface fluxes of sensible heat (F_{sh}, W m^{-2}; yellow), latent heat (F_{lh}, W m^{-2}; cyan), net longwave irradiance (F_{lw}, W m^{-2}; magenta) and net shortwave irradiance (F_{sw}, W m^{-2}; blue); (b1) the height to the maximum specific humidity (h_{sh}) and temperature (h_t); (c1) liquid water path (LWP; g m^{-2}), ice water path (IWP; g m^{-2}) and total water path (TWP; g m^{-2}); (d1) the cloud radiative effect by longwave (F_{lw_CRE}; magenta), with the downstream northward distance from sea-ice edge, along the trajectory of WaMAI in category of RAD over the Barents Sea. (a2)(b2)(c2)(d2) ((a3)(b3)(c3)(d3)) are the same but for WaMAIs in category of TBL (TCD).

694